Actuator Line Simulations of Wind Turbine Wakes Using the Lattice Boltzmann Method

Henrik Asmuth[1], Hugo Olivares-Espinosa[1], and Stefan Ivanell[1]

[1]Uppsala University, Department of Earth Sciences, Wind Energy Campus Gotland, 621 67 Visby, Sweden

Correspondence: Henrik Asmuth (henrik.asmuth@geo.uu.se)

Abstract. The presented work investigates the potential of large-eddy simulations (LES) of wind turbine wakes using the cumulant lattice Boltzmann method (CLBM). The wind turbine is represented by the actuator line model (ALM) that is implemented in a GPU-accelerated (Graphics Processing Unit) lattice Boltzmann framework. The implementation is validated and discussed by means of a code-to-code comparison to an established finite-volume Navier-Stokes solver. To this end, the ALM
5 is subjected to a uniform laminar inflow while a standard Smagorinsky sub-grid scale model is employed in both numerical approaches. The comparison shows a good agreement in terms of the blade loads and near-wake characteristics. The main differences are found in the point of laminar-turbulent transition of the wake and the resulting far-wake. In line with other studies these differences can be attributed to the different orders of accuracy of the two methods. In a second part the possibilities of implicit LES with the CLBM are investigated using a limiter applied to the third-order cumulants in the scheme's collision
10 operator. The study shows that the limiter generally ensures numerical stability. Nevertheless, a universal tuning approach for the limiter appears to be required, especially for perturbation-sensitive transition studies. In summary, the range of discussed cases outline the general feasibility of wind turbine simulations using the CLBM. In addition, it highlights the potential of GPU-accelerated LBM implementations to significantly speed up LES in the field of wind energy.

1 Introduction

15 Large-Eddy Simulations (LES) can provide valuable insights into the aerodynamic interaction of wind turbines. In comparison to modelling approaches of lower fidelity, LES allow for the investigation of aerodynamic effects that are directly associated with the transient nature of highly turbulent flows as found in the atmospheric boundary layer (ABL). Resolving the transient large energy-containing turbulent structures does, however, come at a high computational cost that is far beyond, for instance,
20 Reynolds-averaged approaches (RANS; Mehta et al., 2014). Still, in recent years, LES are increasingly used in engineering-driven contexts. Such are for instance the investigation of fatigue loads in various operating conditions (Storey et al., 2016; Nebenführ and Davidson, 2017; Meng et al., 2018), the effects of turbine curtailment (Nilsson et al., 2015; Fleming et al., 2015; Dilip and Porté-Agel, 2017) or the development and testing of farm-wide optimisation control strategies (Ciri et al.,

2017; Munters and Meyers, 2018). With such applications the computational demand of typical case studies increases dramatically when compared to the more fundamental investigations performed in earlier years of LES of the ABL. This increase in computational demand relates both to the size of considered domains as well as the physical time simulated. Examples of the former are simulations of entire offshore wind farms (Churchfield et al., 2012b; Abkar and Porté-Agel, 2013; Nilsson et al., 2015) or large areas of complex orography (Ivanell et al., 2018; Fang et al., 2018). An extreme example of the latter is the work by Abkar et al. (2016) investigating the wakes in a wind farm throughout two diurnal cycles.

Despite the growing capacities of modern high-performance computing (HPC) clusters, computational power remains the biggest bottleneck for such large scale LES applications. Over the last three decades the Lattice Boltzmann Method (LBM) has evolved into a viable alternative to classical CFD approaches with significantly increased computational performance (Malaspinas and Sagaut, 2014; Krüger et al., 2016). This mostly relates to the strict separation of non-linear and non-local terms allowing for excellent parallelisability (Succi, 2015). The LBM therefore also proves to be perfectly suitable for implementations on Graphics Processing Units (GPU). Various authors documented the substantial speed-up factors of such implementations, see, e.g., Schönherr et al. (2011), Obrecht et al. (2013) or Onodera and Idomura (2018), to name a few. Nevertheless, applications of the LBM in the field of ABL flows and wind energy are still rare compared to other fields of fluid dynamics. To date, one of the few prominent applications in the wider field of atmospheric flows are wind comfort assessments and pollution dispersion in urban canopies (e.g., King et al., 2017; Ahmad et al., 2017; Jacob and Sagaut, 2018; Lenz et al., 2019; Merlier et al., 2018, 2019). Other related applications are wind load assessments as presented by Andre et al. (2015), Fragner and Deiterding (2016) or Mohebbi and Rezvani (2018). In the field of wind energy though, the use of the LBM remains rather limited. Deiterding and Wood (2016), Khan (2018) and Zhiqiang et al. (2018) presented simulations of geometrically resolved model-scale wind turbines. Avallone et al. (2018) and van der Velden et al. (2016) on the other hand investigated noise emissions of blade sections. Various fundamental aspects of the LBM in the context of wind energy and particularly wind farm simulations therefore remain untouched, yet crucial for future applications.

One method of special importance for the modelling of wind turbines in LES is the Actuator Line Model (ALM). The ALM as well as other actuator-type models couple a CFD simulation to an extension of the Blade Element Momentum (BEM) method. Using the locally sampled flow velocity, body forces of a blade element are computed using empirically determined lift and drag coefficients of the referring airfoil section. These are then again applied in the domain of the CFD simulation (Sørensen and Shen, 2002; Troldborg et al., 2010). This avoids prohibitively expensive geometrically resolved simulations of the rotor. It is therefore the only feasible way to represent wind turbines in LES on a wind farm scale today (Sanderse et al., 2011; Mehta et al., 2014). Again, fundamental investigations of the ALM in lattice Boltzmann frameworks are still limited, yet crucial for future simulations of entire wind farms. Rullaud et al. (2018) presented a first conceptual study of the ALM in this context. The presented ALM for vertical axes wind turbines was, however, limited to two dimensions, i.e. cross-sectional planes. More recently, Asmuth et al. (2019) presented an initial fundamental investigation of the classical ALM for horizontal axis turbines in a cumulant lattice Boltzmann framework in uniform laminar inflow. Main aspects of the study were the sensitivity of the blade forces of the ALM to the spatial and temporal resolution of the bulk scheme as well as computational performance.

The objective of this paper is to analyse the wake of a single wind turbine simulated with the ALM and the cumulant lattice Boltzmann method (CLBM), a recently developed high-fidelity collision operator, particularly suited for high Reynolds number flows (Geier et al., 2015, 2017b). The presented analysis covers two main aspects. First, the aforementioned validation study of this ALM implementation (Asmuth et al., 2019) shall be extended to the near- and far-wake characteristics. As a reference

5   we consult the solution of a standard finite volume (FV) Navier-Stokes (NS) solver. For the sake of comparability, this code-to-code comparison is performed using a uniform laminar inflow. By doing so, we follow a similar approach as several other code-to-code comparisons, see, for instance, Sarlak et al. (2015a, b) or Martínez-Tossas et al. (2018). The simplicity of the set-up eliminates various uncertainties associated with more complex, yet, possibly more realistic inflow conditions. Also, it becomes more straightforward to analyse the effect of the numerical scheme or turbulence model on the downstream evolution

10   of the wake and particularly the onset of turbulence as recently discussed by Abkar (2018). Secondly, we use the same set-up to evaluate the impact of turbulence modelling on the solution of the cumulant LBM. Here, we compare the use of an explicit sub-grid scale closure, namely a standard Smagorinsky model, with an implicit LES approach realised by means of a limiter within the collision operator. Lastly, the explicit and implicit approach are also compared in a turbulent inflow that is prescribed using the method by Mann (1998).

15   To the authors' knowledge, this study constitutes the first application of the CLBM to wind turbine wake simulations. Moreover, application-oriented studies of the utilized parametrised version of this collision operator (as further outlined in Sect. 2) are generally still limited, see Lenz et al. (2019). A further motivation of this study is therefore to show the general potential of wind turbine wake simulations using the LBM and specifically the CLBM. The numerical stability of such simulations using the LBM is not self-evident when using typical, rather coarse grid resolutions.

20   The remainder of the paper is organised as follows: Sect. 2 provides a brief introduction to the LBM. This includes a description of the underlying numerical concept, characteristics of the cumulant collision model, the use of turbulence models in the CLBM and, lastly, details on the implementation of the ALM. Sect. 3 describes the utilised numerical frameworks and case set-up. In Sect. 4 we present the code-to-code comparison of this CLBM-ALM to the NS reference case. Sect. 5 covers the discussion of the effects of turbulence modelling on the wake characteristics. In Sect. 6 we shall briefly touch upon aspects

25   of computational performance. Lastly, final conclusions and guidelines for future studies are provided in Sect. 7.

2   The Lattice Boltzmann Method

In the following we provide a brief description of the LBM. This comprises a description of the governing equations as well as more specific topics relevant for the presented studies, such as sub-grid scale modelling and the implementation of the ALM. For a more detailed description of the fundamentals the interested reader is referred to the work by Krüger et al. (2016).

30   2.1   Governing Equations

The LBM solves the kinetic Boltzmann equation, i.e. the transport equation of particle distribution functions (PDF) f in physical and velocity space. PDFs describe the probability to encounter a particle (mass) density of velocity $\boldsymbol{\xi}$ at time t at
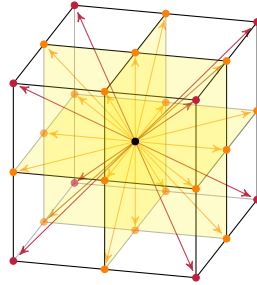
Figure 1. Schematic of three-dimensional velocity lattices. Coordinate-normal planes marked in yellow. The D3Q19 lattice (Qian et al., 1992), with 19 discrete velocity directions given by orange vectors. Additional velocity directions considered in the D3Q27 lattice given by red vectors.

location $\boldsymbol{x}$. Solving the kinetic Boltzmann equation thus requires a discretisation in both physical and velocity space. Using a finite set of discrete velocities (referred to as velocity lattice, see, Fig. 1) and discretising in space and time one obtains the lattice Boltzmann equation (LBE)

$$f_{ijk}(t + \Delta t, \boldsymbol{x} + \Delta t\, \boldsymbol{e}_{ijk}) - f_{ijk}(t, \boldsymbol{x}) = \Omega_{ijk} \tag{1}$$

5 where $\boldsymbol{e}_{ijk} = i\boldsymbol{e}_x + j\boldsymbol{e}_y + k\boldsymbol{e}_z$ is the referring particle velocity vector of each discrete lattice direction. The collision operator Ω_{ijk} on the right-hand side models the redistribution of f through particle collisions within the control volume. Further details thereupon will be given later. The lattice velocity c is chosen such that

$$c = \Delta x / \Delta t = 1 \qquad . \tag{2}$$

On uniform Cartesian grids PDFs are therefore inherently advected to the neighboring lattice node during one time step,
10 explaining the simplicity and explicitness of Eq. (1). The necessary scaling of macroscopic quantities to comply with Eq. (2) will be outlined in Sect. 2.2. Generally, macroscopic variables can be simply obtained from the raw velocity moments of the PDFs

$$m_{\alpha\beta\gamma} = \sum_{ijk} i^\alpha j^\beta k^\gamma\, f_{ijk} \tag{3}$$

with α, β and γ denoting the order of the moment in the referring lattice direction. Following dimensional analysis the macro-
15 scopic mass density ρ is given by the zeroth-order moment m_{000}. Analogously, the momentum in x, y and z is obtained from the first-order moment in the referring coordinate direction m_{100}, m_{010} and m_{001}, respectively.

Based on kinetic theory the collision process is modelled as a relaxation of particle distribution functions towards an equilibrium. In the classical and most simple collision model, the single-relaxation-time model (SRT), commonly referred to as lattice Bhatnagar-Gross-Kroog (LBGK) model (Bhatnagar et al., 1954), all PDFs are relaxed towards an equilibrium using a
20 single constant relaxation time τ, viz.

$$\Omega_{ijk} = -\frac{\Delta t}{\tau}\left(f_{ijk} - f_{ijk}^{eq}\right) = -\frac{\Delta t}{\tau} f_{ijk}^{neq} \quad , \tag{4}$$

with the equilibrium distribution f_{ijk}^{eq} being the second-order Taylor expansion of the Maxwellian equilibrium and f_{ijk}^{neq} referring to the non-equilibrium part of the distribution functions. A Chapman-Enskog expansion of the LBE reveals that

$$\tau = \frac{1}{\omega} = 3\nu/c^2 + \Delta t/2 \quad , \tag{5}$$

with ν being the shear viscosity (He and Luo, 1997; Dellar, 2001).

5   Due to poor numerical stability of the original LBGK model, various alternative approaches have been presented. These mostly relate to the class of multiple-relaxation-time models (MRT), see for instance Lallemand and Luo (2000) and d'Humières et al. (2002). MRT models transform the pre-collision PDFs into a velocity moment space. Each moment can then be relaxed towards a referring equilibrium moment $m_{\alpha\beta\gamma}^{eq}$ with an individual relaxation time. Subsequently the moments are transformed back into particle distribution space and advected. Despite significant stability improvements, several fundamental deficiencies

10   of MRT models render the approach unsuitable for high Reynolds number flows as required for studies of wind turbines in the ABL. Referring to the seminal paper by Geier et al. (2015) such are, among others, the lack of a universal formulation for optimal collisions rates, deficiencies stemming from the rather arbitrary choice of moment space, lacking Galilean invariance and the introduction of hyper-viscosities. Deteriorations of the flow field through local instabilities can be the consequence (Gehrke et al., 2017). To remedy the aforementioned deficiencies Geier et al. (2015) suggest a universal formulation based on

15   statistically independent observable quantities of the PDFs, i.e., cumulants. After performing the two-sided Laplace-transform of the PDFs

$$F(\boldsymbol{\Xi}) = \mathcal{L}(f(\boldsymbol{\xi})) = \int\limits_{-\infty}^{\infty} f(\boldsymbol{\xi}) e^{-\boldsymbol{\Xi}\cdot\boldsymbol{\xi}} d\boldsymbol{\xi} \quad , \tag{6}$$

with $\boldsymbol{\Xi} = \{\Xi, \Upsilon, Z\}$ denoting the particle velocity $\boldsymbol{\xi} = \{\xi, \upsilon, \zeta\}$ in wave number space, cumulants $c_{\alpha\beta\gamma}$ can be obtained as

$$c_{\alpha\beta\gamma} = c^{-\alpha-\beta-\gamma} \frac{\partial^\alpha \partial^\beta \partial^\gamma}{\partial\Xi^\alpha \partial\Upsilon^\beta \partial Z^\gamma} \ln\left(F(\Xi, \Upsilon, Z)\right) \quad . \tag{7}$$

20   Subsequently, cumulants are relaxed towards the referring equilibrium:

$$c_{\alpha\beta\gamma}^* = \omega_{\alpha\beta\gamma} c_{\alpha\beta\gamma}^{eq} + (1 - \omega_{\alpha\beta\gamma}) c_{\alpha\beta\gamma} \quad . \tag{8}$$

Here, $c_{\alpha\beta\gamma}^*$ denotes the post-collision cumulant and $\omega_{\alpha\beta\gamma}$ the referring relaxation rate. As shown by Geier et al. (2015), the statistical independence of cumulants unconditionally eliminates the MRT's deficiencies such as the dependency of Galilean invariance and occurence of hyper-viscosities on the choice of relaxation rates.

25   A simple and widely adopted choice in the CLBM is to set all relaxation rates of higher-order cumulants to one, commonly reffered to as ALLONE cumulant. In this case, higher-order cumulants are instantly relaxed towards the referring equilibrium. This unconditionally damps all higher-order perturbations providing an inherently stable solution and thereby an extremely robust numerical framework. Numerous studies have shown that the ALLONE CLBM can be readily applied to high Reynolds number flows (see, Geier et al., 2015; Far et al., 2016; Gehrke et al., 2017; Kutscher et al., 2018; Onodera and Idomura, 2018). A

30   further development of the original ALLONE is the parametrised CLBM presented in Geier et al. (2017b). Based on the theory

of the so-called *magic parameter* (Ginzburg and Adler, 1994; Ginzburg et al., 2008) the authors derived a parametrisation to optimise the higher-order relaxation rates. The same authors show that the parametrisation increases the convergence of the CLBM in diffusion to fourth order under diffusive scaling (i.e., $\Delta t \propto \Delta x^2$). However, unconditional numerical stability is no longer guaranteed and requires the use of a limiter as outlined in Sect. 2.3.

5   From a theoretical point of view the parametrised CLBM can arguably be seen as one of the most advanced collision models today, both in terms of accuracy and stability. Nevertheless, the complexity of the collision model as well as the use of a D3Q27 velocity lattice make it more demanding in terms of computational and memory demand compared to SRT and MRT models on D3Q19 lattices. In addition to the aforementioned theoretical considerations we therefore provide a pre-study on the suitability of other collision models for this application in Appendix A.

10   2.2   Scaling and Accuracy of the LBM

In order to fulfil the aforementioned requirements of the LBE, physical units need to be rescaled to non-dimensional lattice units (hereafter indexed $(\cdot)^{LB}$), i.e. $c = \Delta x^{LB}/\Delta t^{LB} = 1$. Hence, scaling factors C for all relevant physical units can be derived via non-dimensional quantities. As the LBM generally states a weakly compressible method, these are the Reynolds and Mach number Re and Ma, respectively. Within this study we use the cell Reynolds number as $\mathrm{Re}_c = u_0 \Delta x/\nu$, where u_0 is the inflow

15   velocity and Δx grid spacing. The Mach number is consequently given by u_0 and the lattice speed of sound: $\mathrm{Ma} = u_0/c_s$. Starting from the spatial scaling factor we obtain $C_x = \Delta x/\Delta x^{LB} = L_i/n_i$, where L_i is the length of the domain and n_i the number of grid points in the referring spatial dimension. With $c_s^{LB} = c/\sqrt{3}$, the reference velocity on the lattice is given by $u_0^{LB} = Ma/\sqrt{3}$, yielding the velocity scaling factor $C_u = \sqrt{3}u_0/Ma$. It follows that the temporal scaling factor is given by $C_t = C_x/C_u$, which implies a physical time step $\Delta t = C_t \Delta t^{LB}$ that is inherently proportional to the grid spacing and Mach

20   number. The viscosity in lattice units becomes $\nu^{LB} = \nu C_t/C_x^2$. The order of magnitude of ν^{LB} thus directly depends on the choice of grid resolution and Mach number.

    In this study we employ the LBM for an incompressible problem. As in the majority of applications, this implies that compressibility effects are assumed to have negligible effects on the flow physics of interests. The Mach number is thus merely required to be small, yet, does not have to comply with the physically correct value of the problem. It therefore reduces to a

25   somewhat free parameter affecting numerical accuracy in the incompressible limit (Dellar, 2003; Geier et al., 2015, 2017b), computational demand by means of the time step as well as the magnitude of the viscosity on the lattice level.

2.3   Sub-grid Scale Modelling in the LBM

Early on, LES approaches have been used in LBM frameworks (see, e.g., Hou et al., 1996). The most common choice are eddy-viscosity approaches that are simply adopted from NS frameworks and incorporated by adding the eddy-viscosity ν_t to the

30   shear viscosity ν in Eq. (5). Examples thereof range from the standard Smagorinsky model (Hou et al., 1996; Krafczyk et al., 2003) to more advanced models like the wall-adapting local eddy-viscosity model (WALE; Weickert et al., 2010), the shear-improved Smagorinsky model (SISM; Jafari and Mohammad, 2011) as well as dynamic Smagorinsky approaches (Premnath

et al., 2009b). Others, on the other hand, suggested LB-specific methods based on the approximate deconvolution of the LBE itself (Sagaut, 2010; Malaspinas and Sagaut, 2011; Nathen et al., 2018).

2.3.1 Implementation of Eddy-viscosity Models

The eddy-viscosity can be determined locally using the well-known formulation

$$\nu_t = (C_s \Delta)^2 \bar{S} \quad , \tag{9}$$

where C_s is the Smagorinsky constant, Δ the filter width (here referring to the grid spacing Δx) and $\bar{S}$ the second invariant of the filtered strain rate tensor

$$\bar{S}_{ij} = \frac{1}{2}\left(\frac{\partial \bar{u}_i}{\partial x_j} + \frac{\partial \bar{u}_j}{\partial x_i}\right) \quad , \text{with} \quad \bar{S} = \sqrt{2\,\bar{S}_{ij}\bar{S}_{ij}} \quad . \tag{10}$$

A clear advantage of the LBM over NS approaches in this context is the local availability of the strain rate tensor. Using the second-order moments or cumulants of the local PDFs, respectively, the components of $\bar{S}_{ij}$ can be determined without finite differencing. A detailed description of the determination of $\bar{S}_{ij}$ in cumulant space is provided in Appendix B. It should be noted though that the strain rates in the CLBM and most MRT models are dependent on the total shear viscosity ($\nu_{tot} = \nu + \nu_t$) *and the bulk viscosity*. As opposed to the SRT, where $\bar{S}_{ij}$ is only dependent on the total shear viscosity, it is therefore not possible to explicitly determine ν_t. Hence, the eddy-viscosity $\nu_t(t)$ can be computed either explicitly, using $\nu_t(t - \Delta t)$ or, iteratively. Yu et al. (2005), however, showed that the error associated with the implicitness of ν_t is generally negligible due to the typically small time steps used in the LBM. We shall therefore refrain from implicitly solving for ν_t, in line with similar Smagorinsky approaches in MRT frameworks (Yu et al., 2006; Premnath et al., 2009a).

2.3.2 Implicit LES using the Cumulant LBM

A crucial characteristic of the CLBM is the model's inherent numerical stability. Even for under-resolved highly turbulent flows it does not require the stabilising features of explicit turbulence models. The stabilising characteristic of the original AL-LONE cumulant approach appears rather obvious as it unconditionally resets all higher-order cumulants in each time step. The fourth-order accuracy of the parametrised approach, however, relies on the temporal memory of these higher-order cumulants. Therefore, Geier et al. (2017b) suggest the use of a limiter that is only applied to the relaxation of the third-order cumulants. The relaxation rates $\omega_m, m \in \{3, 4, 5\}$ are consequently substituted by

$$\omega_\zeta = \omega_m + \frac{(1 - \omega_m)\,|C_\zeta|}{\rho\lambda_m + |C_\zeta|} \quad , \tag{11}$$

where C_ζ refers to a third-order cumulant (or linear combinations thereof, respectively, as outlined in the original paper). Destabilising accumulation of energy in these cumulants is hereby inhibited as ω_ζ approaches 1 for $\rho\lambda_m \ll |C_\zeta|$. Nonetheless, the order of the error introduced by the limiter lies well below the leading error of the LBM itself. The fourth-order accuracy of the scheme is thus not affected. Alike the ALLONE version, the parametrised CLBM can therefore be applied as implicit LES (ILES), yet with a higher order of accuracy. In this study we shall therefore focus on the investigation of the parametrised CLBM.

2.4 Implementation of the Actuator Line Model in Lattice Boltzmann Frameworks

The lattice Boltzmann actuator line implementation used in this study closely follows the original description as presented by Sørensen and Shen (2002). The forces acting on the rotor are determined using the local relative velocity u_{rel} of the referring blade elements along the actuator line. The relative velocity is computed from the sampled velocity in blade-normal (stream-

5   wise) and tangential direction u_n and u_θ, respectively using

$$u_{rel} = \sqrt{u_n^2 + (\Omega r - u_\theta)^2} \quad , \tag{12}$$

where Ω is the rotational velocity of the turbine and r the radial position of the blade element. The local blade force per unit length then reads

$$\boldsymbol{F} = 0.5 \rho u_{rel}^2 c (C_L \boldsymbol{e}_L + C_D \boldsymbol{e}_D) \quad , \tag{13}$$

10   with c being the chord length. The lift and drag coefficients C_L and C_D are provided from tabulated airfoil data as functions of the local angle of attack and Reynolds number. The resulting blade forces are subsequently applied across a volume in the flow field by taking the convolution integral of $\boldsymbol{F}$ with a Gaussian regularisation kernel η_ϵ, given by

$$\eta_\epsilon = \frac{1}{\pi^{3/2} \epsilon^2} e^{-(d/\epsilon)^2} \quad , \tag{14}$$

where ϵ adjusts the width of the regularisation and d is the distance to the centre of the blade element. The resulting force is

15   applied at each grid node by simply adding the referring component of $\Delta t / 2 F$ to the pre-collision first-order cumulants. For the sake of completeness it should be noted that body force formulations generally depend on the collision model. See, for instance, Buick and Greated (2000) and Guo et al. (2008) for a description in SRT and MRT frameworks, respectively.

Differences between ALM implementations in NS and LBM frameworks are obviously small. The latter can be expected given that the link between the model itself and the flow solver is simply made by exchanging information of velocity and

20   body forces. Lastly, it is worth mentioning that the locality of all subroutines of the ALM allows for a perfect parallelisation. The model is therefore efficiently parallelised on the GPU, in line with the general architecture of the utlised LBM solver (see Sect. 3.1) using Nvidia's CUDA toolkit.

3   Numerical Set-up

In light of the code-to-code comparison the simulations in both frameworks were set-up in the most similar manner possible.

25   This refers to the grid, the boundary conditions as well as the implementation of the ALM. Nevertheless, certain differences remain unavoidable due to the inherently different numerical approaches. Further details thereupon as well as the set-up in general will be given in the following.

3.1 The Lattice Boltzmann Solver ELBE

The LBM simulations are performed using the GPU-accelerated Efficient Lattice Boltzmann Environment ELBE[1] (Janßen et al., 2015) mainly developed at Hamburg University of Technology (TUHH). The toolkit comprises various collision models, allows for free-surface modelling (Janßen et al., 2017) as well as efficient geometry mapping (Mierke et al., 2018). The implementation
5 of the CLBM in ELBE was recently validated by Gehrke et al. (2017, 2020).

Symmetry boundary conditions (zero gradient with no penetration) are applied at the lateral boundaries of the domain, referring to a simple-bounce back with reversed tangential components (Krüger et al., 2016). The velocity at the inlet is prescribed using a Bouzidi-type boundary condition (Bouzidi et al., 2001; Lallemand and Luo, 2003), i.e., a simple bounce-back scheme adjusted for the momentum difference due to the inlet velocity. For the outlet we chose a linear extrapolation
10 anti-reflecting boundary condition as described in Geier et al. (2015).

3.2 ELLIPSYS3D

As a NS reference we consult the multi-purpose flow solver ELLIPSYS3D developed at the Technical University of Denmark (DTU) by Michelsen (1994a, b) and Sørensen (1995). The code has been applied to numerous wind power related flow problems and served for several fundamental investigations of the ALM (Sørensen and Shen, 2002; Troldborg, 2008; Troldborg
15 et al., 2010; Sarlak et al., 2015a).

The governing equations are formulated in a collocated finite-volume approach. Diffusive and convective terms are discretised using second-order central differences and a blend of third-order QUICK (10%) and fourth-order central differences (90%), respectively. The blended scheme for the convective term was shown to provide sufficient numerical stability while keeping numerical diffusion to a minimum (Troldborg et al., 2010; Bechmann et al., 2011). The pressure correction is solved
20 using the SIMPLE algorithm. Pressure decoupling is avoided using the Rhie-Chow interpolation.

Symmetry conditions are applied at the lateral boundaries, equivalently to the LB set-up. The outlet boundary condition prescribes a zero velocity gradient.

3.3 Case Set-up

For the evaluation of the ALM we choose one of the most prominent test cases in this context, i.e. the simulation of the NREL
25 5MW reference turbine (Jonkman et al., 2009) subjected to an inflow velocity of $u_0 = 8\,\mathrm{m\,s^{-1}}$ and operating at optimal tip-speed ratio of $\lambda = 7.55$. With the viscosity of air $\nu = 1.78 \cdot 10^{-5}\,\mathrm{m^2\,s^{-1}}$ the Reynolds number with respect to the diameter D amounts to $\mathrm{Re}_D = u_0\,D/\nu = 5.7 \cdot 10^7$ (with $D = 126\mathrm{m}$). The rectangular computational domain spans $6\,D$ in the cross-stream directions and $29\,D$ in the stream-wise direction. For the sake of comparability, the grid is uniformly spaced in the entire domain. The turbine is located laterally centred $3\,D$ downstream of the inlet. A schematic of the set-up including the definition of coordinates is given in Fig. 2. Based on a prior investigation of the convergence of second-order statistics all simulations are
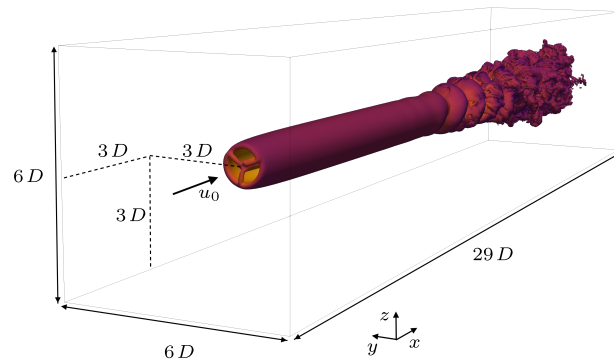
---

[1]https://www.tuhh.de/elbe

Figure 2. Schematic of the case set-up outlining the dimensions of the computational domain, position of the turbine and definition of coordinates.

initially run for 4.39 domain flow-through times. Statistics are subsequently gathered over another 17.52 domain flow-through times.

4   Code-to-code Comparison in Uniform Inflow

As a starting point we compare the results obtained with the CLBM to the NS reference. For this initial investigation a

5   Smagorinsky model is applied in both numerical approaches. The Smagorinsky-constant is set to $C_s = 0.08$, similar to previous studies of the topic (Martínez-Tossas et al., 2018; Deskos et al., 2019). The limiter in the CLBM is set to $\lambda_m = 10^6$ and thus practically switched off. Each model is run with three different grid resolutions $\Delta x = \{D/16, D/24, D/32\}$. This choice of grid resolutions is below values found in fundamental investigations of, for instance, the evolution of tip vortices (Ivanell et al., 2010; Sarmast et al., 2014). Yet, it lies well within the range commonly found in wind farm simulations using the ALM

10   where higher resolutions might be unfeasible, see, e.g., Porté-Agel et al. (2011), Churchfield et al. (2012a), Andersen et al. (2015) or Foti and Duraisamy (2019). Generally, the tip of the actuator line is required not skip a cell in one timestep Δt in order to ensure a continuous coupling of the ALM with the flow field. In NS-based LES this condition dictates the choice of Δt resulting in a Courant-Friedrichs-Lewy number with respect to u_0 of CFL $= 0.132$. Referring to Troldborg et al. (2010), the CFL number is thus typically lower than required by the LES to obtain timestep independence. In LBM simulations the

15   timestep is usually dictated by the Mach number as outlined in Sect. 2.2. Choosing Ma $= 0.1$ we get CFL $= 0.058$ for the CLBM cases. This is obviously well below the value required by the ALM, yet inevitable due to the numerical method.

As for the ALM, the blades in all cases are discretised by 64 points. The smearing width is set to $0.078125\,D$ referring to $\epsilon/\Delta x = \{1.25, 1.875, 2.5\}$ for the three different resolutions, respectively.
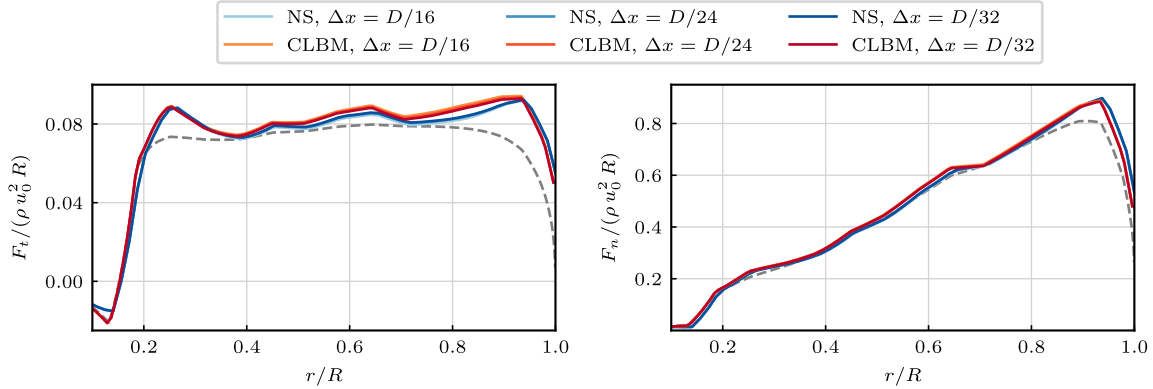
Figure 3. Mean tangential force F_t (left) and normal force F_n (right) along the actuator line. Grey dashed line marking the BEM reference by Hansen (2008).

4.1 Blade Loads

Results of the simulations for the time-averaged tangential and normal force components of all cases are given in Fig. 3. BEM (Blade Element Momentum) computations following Hansen (2008) are provided as an additional reference. It becomes obvious that the dependency of the blade forces on the grid resolution is small in both numerical approaches. The same holds

5   for the differences between the CLBM and the NS solution, even though these are found slightly larger than in the former comparison. The deviations from the BEM reference can be related to the influence of the force smearing as well as the lack of a correction model as discussed by Meyer Forsting et al. (2019). Also, despite the relatively low values for $\epsilon/\Delta x$ in the cases with $\Delta x = \{D/16, D/24\}$, no numerical disturbances were caused by ALM in the NS simulations. Note that some authors recommend $\epsilon/\Delta \geq 2$ in order to avoid spurious oscillations (Jha et al., 2013; Martínez-Tossas et al., 2015). Here, instabilities

10   were only found for $\epsilon/\Delta \leq 1$. The choice of ϵ therefore states a compromise ensuring numerical stability for the cases with lowest resolution while keeping it as low as possible with respect to the cases with the highest spatial resolution. In summary and in line with other similar code-to-code comparisons (Sarlak, 2014; Sarlak et al., 2015b; Martínez-Tossas et al., 2018) it can be concluded that the agreement in the blade forces is sufficient to facilitate a wake comparison with focus on the behaviour of the bulk scheme.

15   ## 4.2 Wake Characteristics

Firstly, we compare the time-averaged cross-stream velocity profiles, given in Fig. 4. It can be seen that the two numerical approaches agree very well in the near-wake of the turbine. The same applies for the observed changes between the grid resolutions. For the stream-wise velocity component we shall quantify this observation by means of the L^1-relative error norm. Specifically, we compute the error $L^1_{ij}(u)$ for the resolved velocity profile of one resolution Δx_i with respect to the next finer
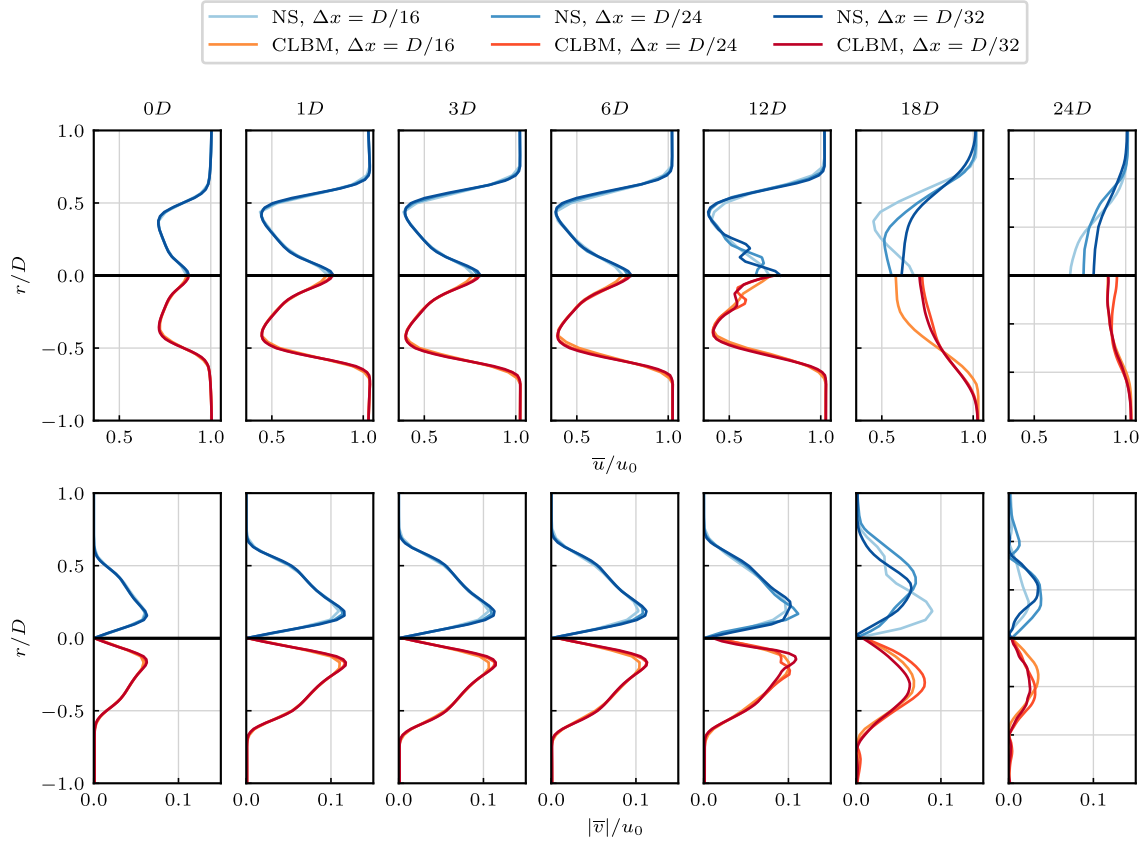
WIND
ENERGY
SCIENCE
DISCUSSIONS

eawe
european academy of wind energy

Open Access

Figure 4. Cross-stream profiles of the mean stream-wise velocity $\overline{u}$ (top) and tangential velocity $\overline{v}$ (bottom) of the CLBM compared to the NS reference cases at different downstream positions.

resolution Δx_j:

$$L_{ij}^1(u) = \frac{1}{n_z} \sum_{k=1}^{n_z} \frac{|\overline{u}_i(z(k)) - \overline{u}_j(z(k))|}{|\overline{u}_j(z(k))|} \quad , \tag{15}$$

where n_z is the amount of sample points along the profile. Furthermore, we provide the order of grid convergence $p(u(z))$ following the method for non-constant refinement ratios as described in Roache (1998), based on the generalised theory of

5   the Richardson extrapolation. It should, however, be noted that $p(u(z))$ of the presented cases should not be interpreted in the classical sense, i.e., as the asymptotic order of convergence of the numerical methods. This would require solutions within the asymptotic range of convergence. Here, it merely serves as a summarising quantity to facilitate the comparison of the two approaches at different grid resolutions. The mean of $p(u(z))$ along the profile $\langle p(u) \rangle$ as well as $L_{ij}^1(u)$ are given in Tab. 1. It can be seen that the differences between the three spatial resolutions in each numerical approach lie indeed very closely

10   within the same order of magnitude, not only for each refinement step but also at each downstream position. Consequently, the

Table 1. Measures of grid convergence $L^1_{ij}(u)$ and $\langle p(u) \rangle$ of the stream-wise velocity profiles in the near-wake. Index $i, j = 1$ referring to the finest grid, 2 and 3 to the middle and coarse grid, respectively.

	x	$0\,D$	$1\,D$	$3\,D$	$6\,D$
$L^1_{21}(u) \cdot 10^{-3}$	NS	4.44	11.84	19.02	33.47
	CLBM	3.06	10.26	16.18	23.55
$L^1_{32}(u) \cdot 10^{-3}$	NS	8.73	23.40	41.61	68.37
	CLBM	6.21	21.06	32.65	46.80
$\langle p(u) \rangle$	NS	1.043	1.072	1.026	0.992
	CLBM	0.950	0.967	1.254	1.060

order of convergence is found to be close to one for both approaches at all positions. In the near-wake region discussed here, viscous effects usually only play a minor role. This shows, for instance, in a small wake recovery with downstream distance. Also, the rotational velocity does not change significantly. The wake is thus mostly governed by the inviscid flow solution (Troldborg, 2008; Troldborg et al., 2010). Both the NS and the CLBM approach recover the Euler equations at the same order

5 of accuracy. A similar numerical behaviour in this part of the wake should therefore be expected (assuming comparability of all other aspects like boundary conditions and the implementation of the ALM). In light of the motivation for this comparison these results can thus be appreciated.

Further downstream ($x > 6\,D$) differences between all compared cases increase significantly. Generally, the vortex-sheet of the near-wake starts to meander and eventually breaks down as the wake transitions to a fully turbulent state. An impression

10 thereof is provided in Fig. 5, showing the downstream evolution of the wake in terms of the contour plots of the instantaneous stream-wise velocity.

After the onset of turbulence the wake starts to recover more rapidly while the turbulence slowly decays. Differences in the velocity in the far-wake both between the two numerical approaches as well as the referring grid resolutions can therefore be related to different downstream positions of the points of transition.

15 More quantitatively, the break-down of the wake can be observed by means of a drastic increase in the turbulence intensity Ti as depicted in Fig. 6. It shows that the turbulence intensity in all CLBM cases lies at a similar magnitude in the near-wake. At the same time it is notably higher than in the NS cases at the same downstream position. Downstream of $x = 6\,D$ it can be seen that Ti generally increases faster with downstream distance the higher the spatial resolution. Also, it increases earlier in the CLBM than in the NS solutions. In addition to Fig. 6 this process is illustrated in Fig. 7 by means of the stream-wise

20 evolution of Ti at a radial position of $r/D = 0.625$. It clearly shows the faster increase of Ti at higher spatial resolutions as well as a downstream shift of the build-up in the NS cases.

The mechanism of the transition of wind turbine wakes has been extensively described based on ALM simulations, see, e.g., Sarmast et al. (2014). Fundamental studies thereof do, however, mostly use higher spatial resolutions in order to resolve distinct tip-vortices. With the resolutions and smearing width used here the wake rather resembles a vortex sheet similarly to
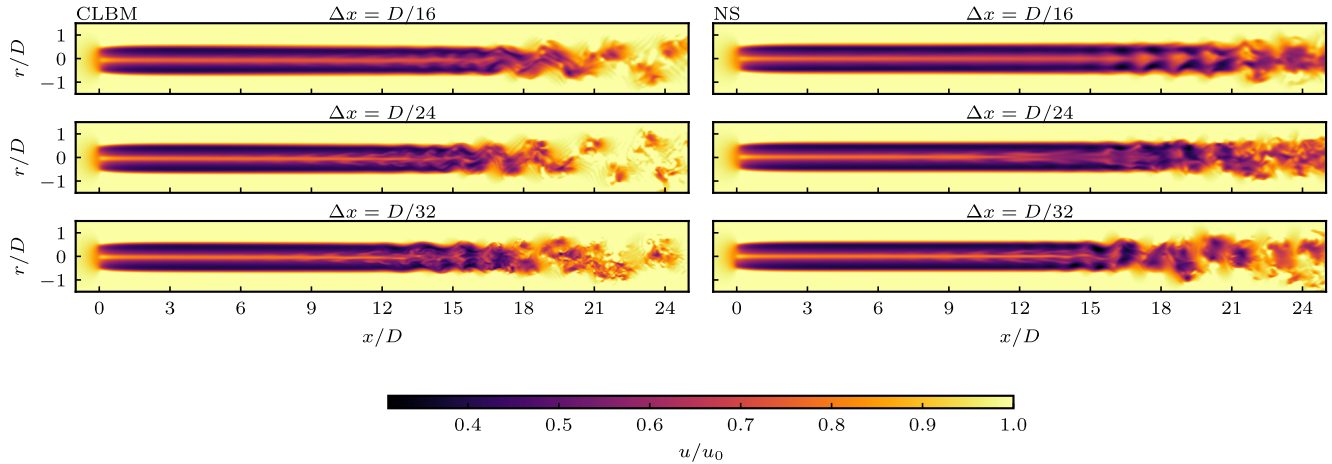
Figure 5. Contour plots of the instantaneous stream-wise velocity u in the central stream-wise plane at different spatial resolutions (top to bottom) with the CLBM (left) and NS (right).
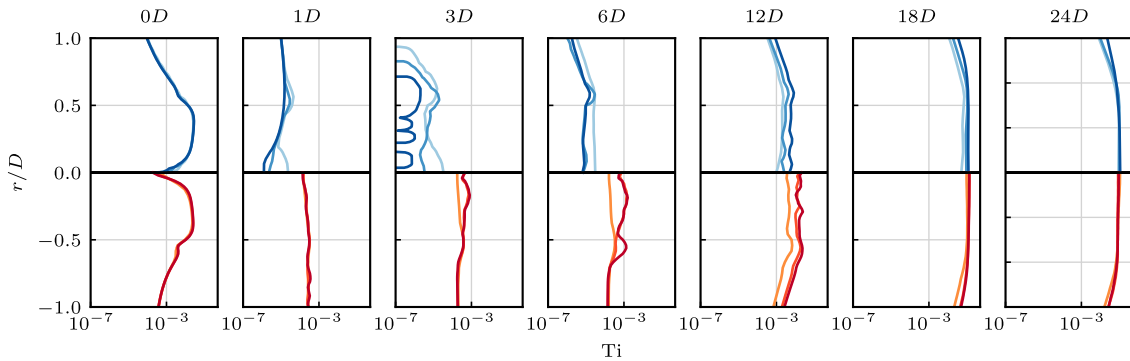

Figure 6. Cross-stream profiles of the turbulence intensity Ti $= \frac{1}{u_0} \sqrt{\frac{1}{3} \overline{u_i' u_i'}}$ of the CLBM compared to the NS reference cases. Please note the log-scale on the abscissa. Gaps in the line plots (e.g. at $x = 3D$) refer to regions of negligible Ti. For legend, see Fig. 4.

actuator disk simulations. To the authors' knowledge only Martínez-Tossas et al. (2018) briefly described the transition process of wakes of such low-resolution ALM. In their discussion of a similar code-to-code comparison the authors argue that small perturbations at high wave numbers eventually trigger the transition of the wake. Schemes with lower numerical diffusivity (pseudo-spectral approaches in that study) generally dampen those perturbations less than more diffusive lower-order schemes (referring to second-order collocated finite-volume discretisations, equivalently to the NS reference used here) and thus show a faster growth of turbulence. The same interpretation can indeed be applied to the results shown here. As described in Sect. 2, the parametrisation of the relaxation rates results in a scheme with fourth-order accuracy in diffusion as opposed to the second-order accuracy of the NS finite-volume scheme. At this point we shall briefly comment on the second-order accurate ALLONE
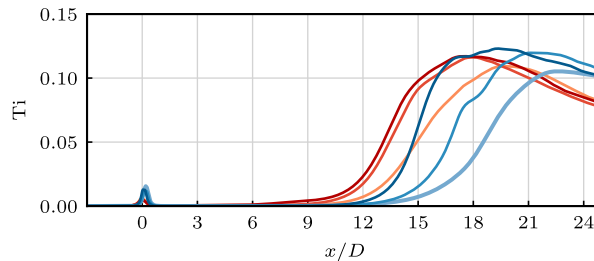
5

Figure 7. Stream-wise evolution of the turbulence intensity Ti at $r/D = 0.625$ in the CLBM and NS cases. For legend, see Fig. 4.

CLBM mentioned earlier (Sect. 2). In fact, using this version of the CLBM the transition behaviour at all resolutions was found to be more similar to the NS solution. This generally corroborates the aforementioned discussion on the effect of the numerical diffusivity. Nevertheless, a further analysis of the ALLONE CLBM is omitted here for the sake of brevity.

As a last aspect of the code-to-code comparison we analyse the one-point turbulence kinetic energy spectra. The spectra shown in Fig. 8 represent the average of sixteen points in the referring cross-sectional plane at a radial position of $r/D = 0.625$. For additional smoothing the Welch method was applied at each point with non-overlapping time intervals of a fifteenth of the overall sampling period.

The energy content in the near-wake ($x = 1\,D$) is expectedly small when compared to the far wake where the vortex sheet has broken down in most of the shown cases. The energy level across most frequencies is indeed low enough to be related to numerical noise making a further interpretation obsolete. The only distinct feature at $x = 1\,D$ are notable peaks at the blade-passing frequency f_B and its higher harmonics. These are found in all presented cases, yet generally slightly smaller in the NS solutions. This signature at f_B was recently described by Nathan et al. (2018) but using twice as many grid points per diameter when compared to the highest resolution shown here. It can thus be appreciated that this transient feature of the ALM remains traceable down to resolutions of $\Delta x = D/16$.

At $x = 12\,D$ a pre-transition wake meandering can be seen. The occurrence of this feature is not as confined to a single frequency as the aforementioned blade-passing frequency. Yet, an increased energy level in a frequency band around $f_m \approx 0.025\mathrm{Hz}$ (and its higher harmonics) can be observed in all cases. It was illustrated in Fig. 5 that the meandering starts to occur at different positions downstream depending on the resolution and numerical approach. It then steadily increases until the wake becomes fully turbulent. The amplitudes at f_m therefore differs depending on how far upstream the meandering started to build up. Also, it again shows that the meandering and subsequent transition occurs earlier in the CLBM cases. Additionally, the signature of the blade passage is still visible in the lower-resolution CLBM cases. This is not the case for the NS reference, despite the smaller meandering at this downstream position. In line with the observations made earlier, this aspect might relate to a higher numerical dissipation of the NS scheme.

Further downstream at $x = 24\,D$ the wake is fully turbulent in all CLBM cases, characterised by a sub-intertial range with typical -5/3-slope. This is also the case for the NS solution with $\Delta x = D/32$. Here, however, the meandering is still more
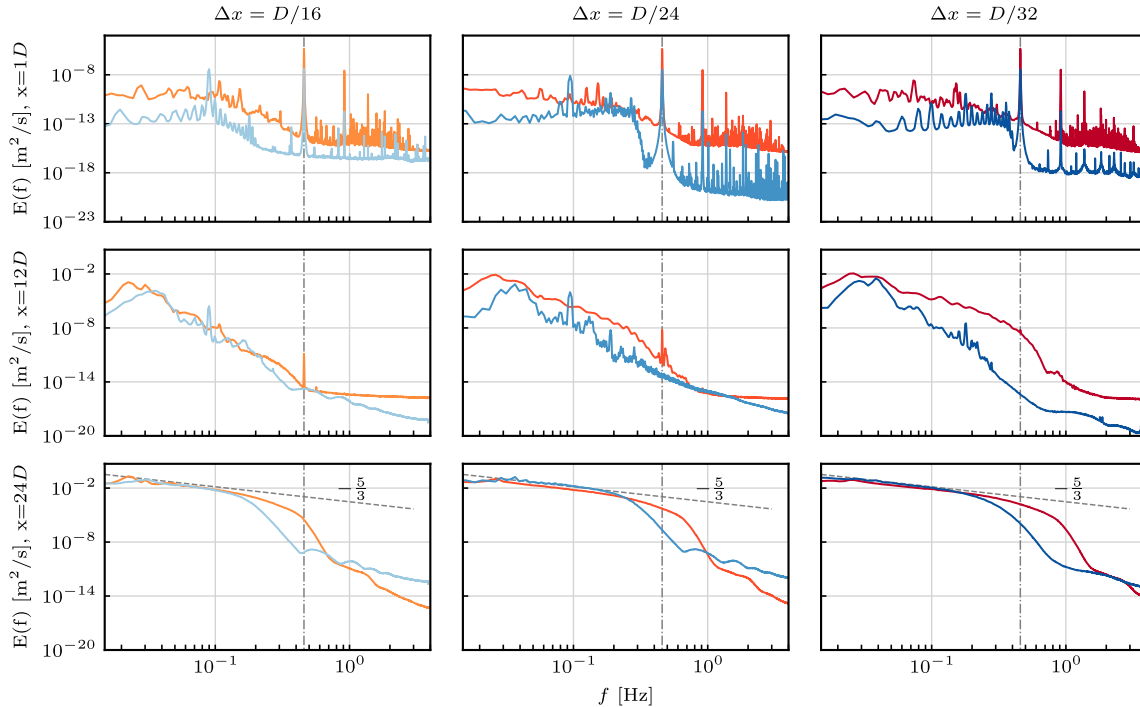
Figure 8. One-point turbulent kinetic energy spectra in the near- ($x = 1\,D$, top) and far-wake ($x = 12\,D$, middle; $x = 24\,D$, bottom) at increasing spatial resolution from left to right. Vertical dashed-dotted line marking the blade-passing frequency $f_B = (3u_0\lambda)/(\pi D) = 0.458$Hz. Mind the change of scale on the y-axis between the first and second row of subplots. For legend, see Fig. 4.

visible due to the later start of the transition of the wake. Also, when comparing both approaches at the highest spatial resolution (bottom right in Fig. 5) it shows that the sub-inertial range of the CLBM approach reaches to higher frequencies. In accordance with that, it appears that the CLBM does indeed resolve smaller turbulent structures, as shown in the contour plot of the Q-criterion (Fig. 9).

4.3 Discussion

The results presented here generally show that the CLBM provides a numerical framework the ALM can be readily applied in. In addition to our previous study (Asmuth et al., 2019) this further validates the LBM-ALM implementation discussed here. Also, it extents previous demonstrations of the robustness of the ALM with respect to the numerical approach to a new model, i.e. the CLBM. In line with the code-to-code comparisons referred to earlier (Sarlak, 2014; Sarlak et al., 2015a, 2016; Martínez-Tossas et al., 2018) we can highlight three main aspects of the comparison: an excellent agreement in the near-wake, differences in the point of transition depending on the order of accuracy in diffusion and, again, a good agreement in the far-wake after the transition.
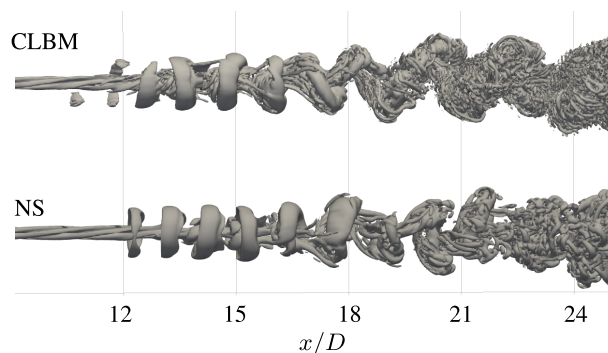
Figure 9. Rendering of the instantaneous contours of the Q-criterion ($Q = 0.0005$) in the far-wake with the CLBM and NS with $\Delta x = D/32$.

5   Comparison of Implicit and Explicit Sub-grid Scale Modelling in the Cumulant LBM

Previous studies have shown that the additional damping introduced by sub-grid scale models can have a significant impact on the point of transition of wind turbine wakes in uniform inflow. See, for instance, the code-to-code comparison studies mentioned above or the recent works by Abkar (2018) or Deskos et al. (2019). The near-wake characteristics as well as the

5   blade loads, on the other hand, are usually not much affected. Conversely, the impact of the turbulence model in turbulent inflow was usually found to be negligible. Here, the ambient turbulence usually states the dominant factor causing the instability of the wake.

With the limiter of the third-order cumulants described in Eq. (11), the CLBM allows for an implicit damping of high-wave number perturbations alternatively to classical turbulence models. Geier et al. (2017b) showed theoretically and by means of a

10   decaying shear-wave and Taylor-Green vortex that the use of the limiter does not affect the asymptotic order of accuracy of the scheme. Investigations of the effects of the limiter in more applied high-Reynolds-number cases are, however, not available to date. Geier et al. (2017a) and Lenz et al. (2019) presented applications of the parametrised CLBM, yet both did not touch upon the topic discussed here. Then again Pasquali et al. (2017) state that they chose suitable values for λ_m manually, close to the stability limit and case-dependent. Both the effect of λ_m on turbulent flows, as well as criteria to choose adequate values thus

15   remain open questions.

In the following we investigate the impact of λ_m on the characteristics of the wake in comparison to the case with Smagorinsky model presented in Sect. 4. For the sake of brevity only a resolution of $\Delta x = D/32$ will be looked at. Three values of λ_m are investigated ranging from 10^0 to 10^{-2}. The former value states the smallest possible to ensure numerical stability. Moreover, in addition to a simple uniform inflow we perform simulations with imposed synthetic turbulence at the inlet.
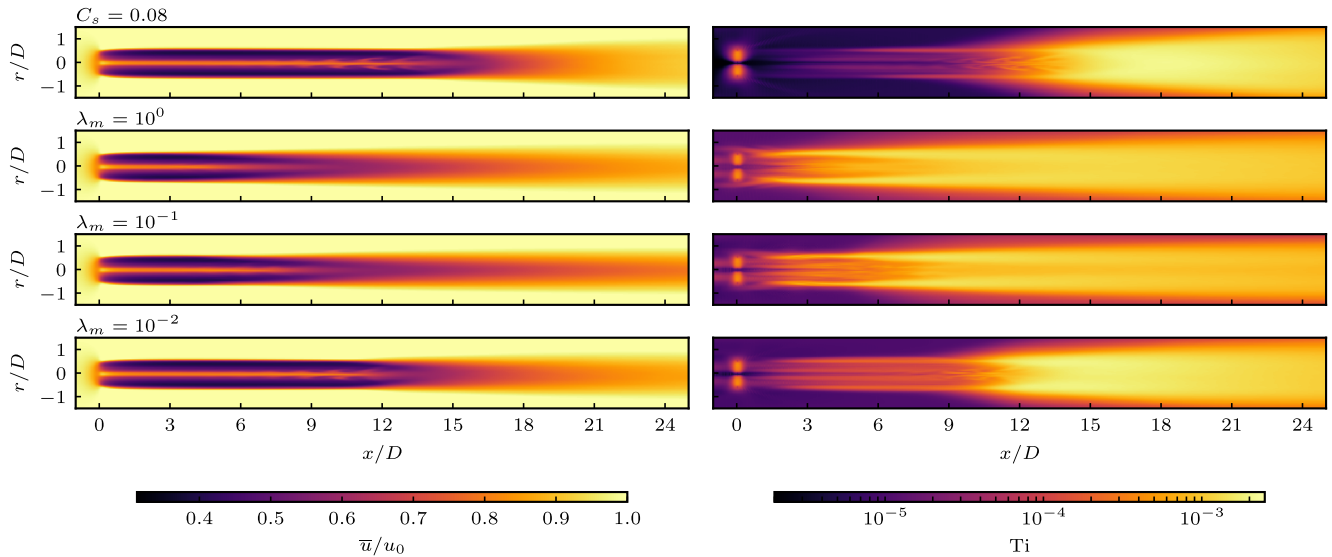
Figure 10. Contour plots of the mean stream-wise velocity $\overline{u}$ (left) and turbulence intensity Ti (right) in the central stream-wise plane in uniform inflow with the CLMB using the Smagorinsky model (top) and different values of the third-order cumulant limiter λ_m (second to last row), repectively.

5.1 Wake Characteristics in Uniform Inflow

To begin with, it should be noted that the impact of the turbulence modelling on the blade loads was found to be negligible. This is in line with many of the aforementioned studies on the topic using NS formulations. A further discussion thereof is thus omitted.

5 Contour plots of the mean stream-wise velocity and turbulence intensity are shown in Fig. 10. While the mean velocity in the region close to the turbine is almost unaffected by the choice of λ_m , the evolution of the turbulence intensity and ultimately the point of transition change drastically. With $\lambda_m = 10^0$, Ti grows significantly closely behind the turbine. Only $3D$ downstream the wake is already highly turbulent (as also shown later in Fig. 11). With $\lambda_m = 10^{-1}$ the wake characteristics only change marginally. Increasing λ_m from 10^{-1} to 10^{-2}, however, delays the transition considerably. This implicitly shows

10 that the order of magnitude of the third-order cumulants in crucial regions of the wake lies within this range, which can be deduced from Eq. (11). When choosing $\lambda_m = 10^{-2}$ the limiter damps the third-order cumulants considerably when compared to the optimised relaxation rates. Moreover, the far-wake distribution of Ti resembles more closely the one of the Smagorinsky case than with lower λ_m. Turbulent perturbations of the wake do, however, grow over a longer fetch than in the Smagorinsky case, starting in the near-wake.
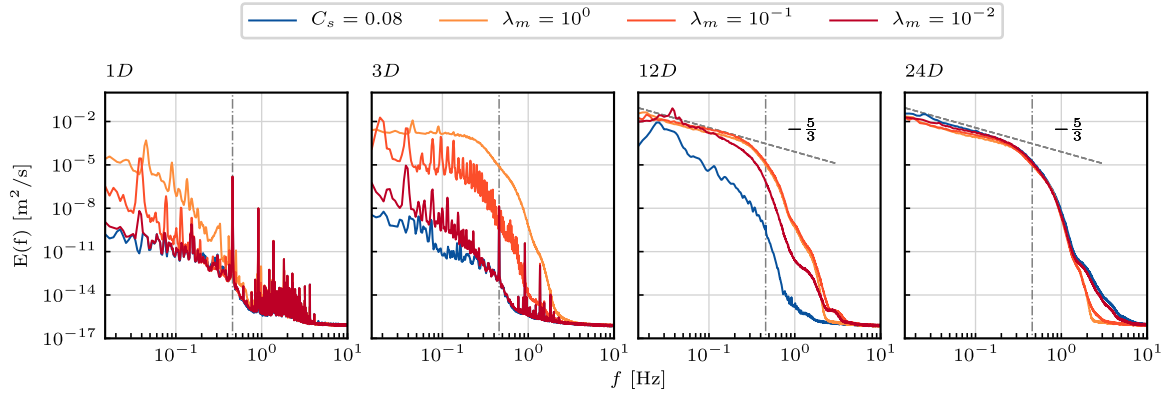
Figure 11. One-point turbulent kinetic energy spectra at different positions downstream. Vertical dashed-dotted line marking the blade-passing frequency f_B.
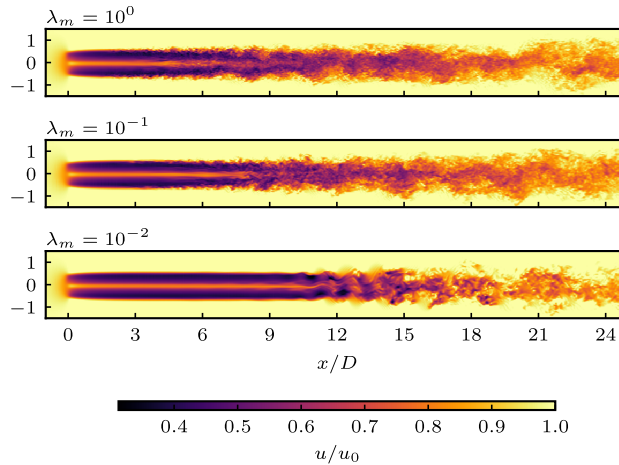

Figure 12. Contour plots of the instantaneous stream-wise velocity u in the central stream-wise plane.

Further insights can again be gained by consulting the spectra of the turbulence kinetic energy, see Fig. 11. It becomes obvious that the turbulent kinetic energy content close to the turbine increases significantly in the near-wake ($x = 3D$) with increasing λ_m. Distinct peaks related to larger meandering scales are again visible. These are, however, increasingly accompanied by energies across all frequencies below f_B the higher λ_m. The pre-transition meandering, as described in Sect. 4.2, and clearly visible for the Smagorinsky case at $x = 12D$ is thus not as significant. The transition to a fully turbulent wake appears to occur too fast for this process to develop. A qualitative impression thereof can be obtained from the instantaneous velocity plots given in Fig. 12. Only with $\lambda_m = 10^{-2}$ a more distinct development of such large meandering structures can again be seen, similarly to the Smagorinsky case.

Lastly, it should be noted that increasing λ_m also increases the amplitude of small scale fluctuations in the ambient flow field. Among others, these are likely to be related to acoustic reflections of small scale turbulence on the domain boundaries and/or spurious numerical oscillations. Partially, these can be seen in the Ti contour plots (Fig. 10) upstream of the turbine for the two higher λ_m values. More specifically, $1\,D$ upstream of the turbine, we find Ti $= \mathcal{O}(10^{-4})$ for $\lambda_m = 10^0$. In comparison,

5   the Smagorinsky case and the NS reference discussed earlier exhibit a magnitude that is two and three orders of magnitude lower, respectively. Referring to the discussions of tip-vortex stability by Ivanell et al. (2010) or Sørensen et al. (2015), an effect thereof on the break-down of the wake can not be ruled out. Unfortunately, most studies similar to the one presented here did not comment on this topic. Deskos et al. (2019), on the other hand, found that the mutual inductance of tip-vortices can be severely disturbed if the diffusivity of the scheme is too low. Further investigations on the effect of the limiter thus remain

10   inevitable.

5.2 Impact of Inflow Turbulence

Previous investigations have found that the effect of the turbulence model on the wake characteristics is almost negligible if the inflow is turbulent (Sarlak et al., 2015a; Martínez-Tossas et al., 2018). For the sake of completeness, we shall therefore perform the same parameter study with imposed synthetic turbulence at the inlet.

15   ### 5.2.1 Synthetic Turbulence Generation at the Inlet

At the inlet we prescribe homogeneous isotropic turbulence (HIT) based on the von Kármán energy spectrum. The three-dimensional field of velocity fluctuations is generated based on the method by Mann (1998) using the open-source code TuGen by Gilling (2009). As we are only interested in HIT the model's shear parameter Γ is set to zero. The length scale of the spectral velocity tensor is chosen as $L = 40\mathrm{m} = 0.317\,D$. The mean turbulence intensity is scaled via the coefficient

20   $\alpha\epsilon^{2/3}$. The length of the turbulence field in the stream-wise direction measures 16384m. Following Taylor's frozen turbulence hypothesis the field is advected with u_0 and superimposed at the inlet. The turbulence field is consequently recycled after 4.48 domain flow-through times. The lateral dimensions of the field are set to 2048m (referring to $16.25\,D$). Since we only use a cross-section of $6\,D \times 6\,D$ we ensure zero correlation of the velocity fluctuations between the lateral boundaries of the domain. The spatial resolution of the field is 8192 grid points in the stream-wise direction and 128 grid points in the lateral directions.

25   In Fig. 13 we compare the stream-wise evolution of the turbulence intensity at hub-height without ALM present. Right behind the inlet we observe a small increase of Ti regardless of the turbulence model. As described by Gilling and Sørensen (2011) and Keck et al. (2014) this relates to the adaptation of the velocity field to discontinuities introduced by the interpolation at the inlet. Thereafter, the turbulence continuously decays due to the absence of mean shear. For the ILES cases we find a turbulence intensity of around 8.5% at the turbine position. The turbulence intensity for the Smagorinsky cases is about 0.5%

30   lower, which can be related to the higher dissipation introduced by the model. Major differences in the spectra of the turbulence kinetic energy at hub height could not be observed, as shown in Fig. 14.
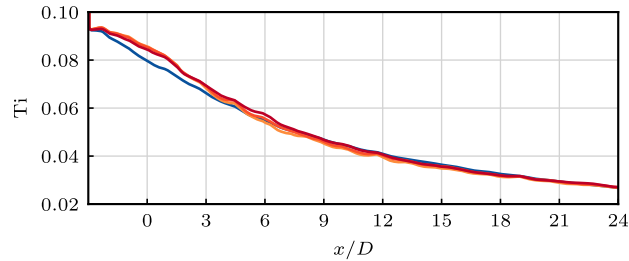
Figure 13. Stream-wise evolution of the turbulence intensity Ti in the domain center with the CLBM without ALM. For legend, see Fig. 11.
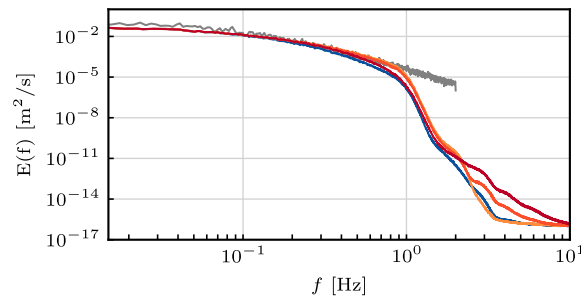

Figure 14. One-point turbulent kinetic energy spectra at the turbine position ($x = 0\,D$) with the CLBM without ALM. The spectrum of the synthetic inlet turbulence is given in grey. For legend, see Fig. 11.

5.2.2 Wake Characteristics

Cross-stream profiles of the mean stream-wise velocity are given in Fig. 15. In contrast to the results in uniform inflow, the influence of the turbulence modelling approach appears small. Generally, the break-down of the wake occurs more closely behind the turbine accompanied by a significantly faster wake recovery than in uniform inflow. Further downstream the wake quickly

5   approaches a self-similar Gaussian profile as described by Sørensen et al. (2015). Equivalently, the turbulence intensity follows a more similar course than in uniform inflow, see Fig. 16. The slightly smaller Ti at the turbine position in the Smagorinsky case can be seen in the wake center up until $x = 1\,D$. Further downstream the turbulence of the wake itself dominates Ti with only small differences towards the ILES cases.

In the turbulent cases shown here the transition of the wake is dominated by the resolved turbulent scales of the incoming

10   flow. The dampening effect of λ_m on smaller scales thereby seems to be negligible for the general evolution of the wake. The effect of the limiter on this particular flow case is thus equally negligible as other sub-grid scales models investigated in NS frameworks (Sarlak et al., 2016; Martínez-Tossas et al., 2018).
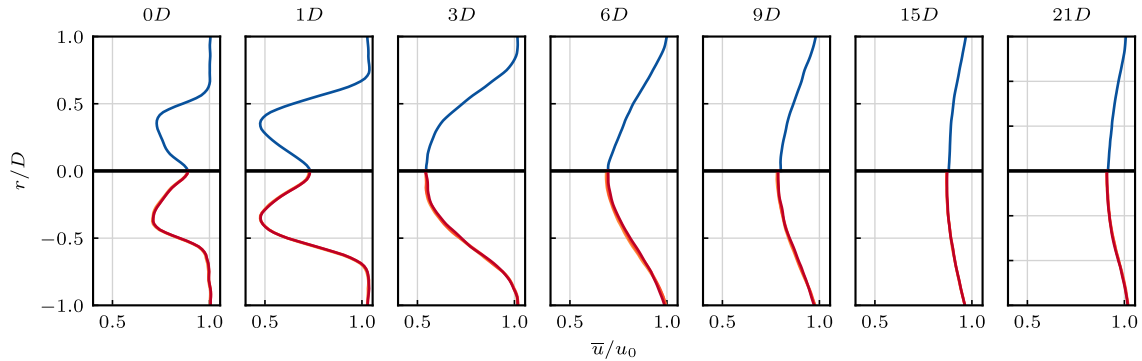
Figure 15. Cross-stream profiles of the stream-wise $\overline{u}$ of the CLBM with different turbulence models in turbulent inflow. For legend, see see Fig. 11.
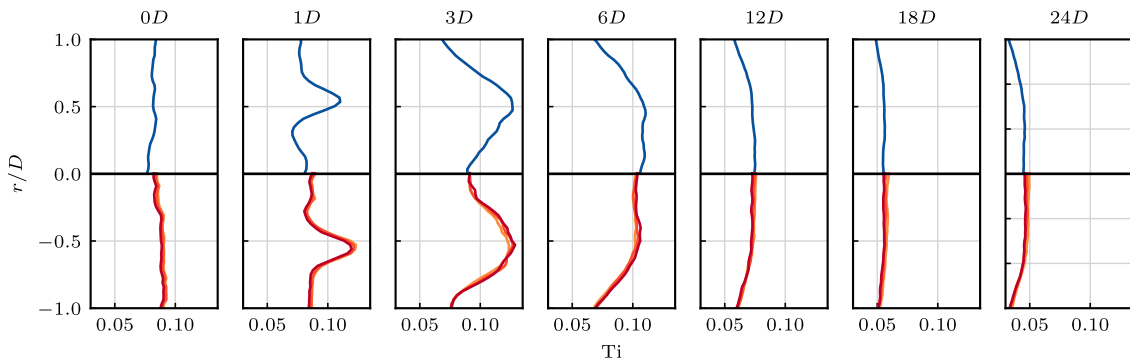

Figure 16. Cross-stream profiles of the turbulence intensity Ti of the CLBM with different turbulence models in turbulent inflow. For legend, see Fig. 4.

6 Computational Performance

We initially outlined that the main motivation for the use of the LBM in this context is the method's superior computational performance. Nevertheless, a detailed discussion is not the focus of this paper. For further details on this topic we refer to our previous study (Asmuth et al., 2019) as well as numerous other publications, see, for instance, Schönherr et al. (2011), Obrecht et al. (2013), Januszewski and Kostur (2014), Hong et al. (2016) or Onodera et al. (2018). In brief, we shall remark that all simulations with the CLBM ran with an average of 1050 MNUPS (Million Node Updates Per Second). A similar single-GPU performance on uniform grids was recently reported by Lenz et al. (2019). For the cases discussed in this study this refers to a wall time of 524s per domain flow-through time on a single Nvidia RTX 2080 Ti on a local workstation. Putting this into perspective, the wall time per flow-through time of the NS case amounts to 5028s. The latter ran on 1044 CPU cores (Intel Xeon

Gold 6130) and thus refers to 1463 CPUh. A last interesting aspect to remark is the ratio of simulated real time to computation time $r_{r2c} = \Delta t_{real}/\Delta t_{comp}$. The topic was recently addressed in the context of urban flows (Onodera and Idomura, 2018; Lenz et al., 2019) as well as for atmospheric boundary layer flows and wind energy applications (Bauweraerts and Meyers, 2019). A ratio of $r_{r2c} > 1$ would enable the use of LES for real-time forecasts of, e.g., urban micro-climates or wind farm

5   performance and loads. For this specific LBM case we obtain $r_{r2c} = 0.902$. For the NS approach we get $r_{r2c} = 0.094$. Despite this obviously only being a case study, real-time LES of wind farms with affordable hardware demand appear possible.

7   Conclusions

The cumulant lattice Boltzmann method was applied to simulate the wake of a single wind turbine. The turbine was represented by the actuator line model. First, the presented model was compared against a well-established finite volume Navier-Stokes

10   solver. It was shown that the cumulant lattice Boltzmann implementation of the actuator line model yields comparable first- and second-order statistics of the wake. The main differences were found in the point of transition depending on the numerical diffusivity of the scheme. Secondly, the impact of the third-order cumulant limiter was investigated in both laminar and turbulent inflow. The latter was prescribed using the method by Mann (1998). As similarly observed in explicit sub-grid scale models, the limiter affected the wake in laminar inflow significantly. Also, it was found that a limiter close to the numerical

15   stability limit, as suggested by others (Pasquali et al., 2017), can lead to spurious oscillations in the ambient flow. Differences in turbulent inflow were then again found to be small. On the one hand, the study shows that the choice of the limiter is by no means irrelevant despite the negligible influence on the asymptotic order of accuracy (Geier et al., 2017b). Likewise, this dampening characteristic clearly shows the potential to be used in a more systematic way as an implicit LES feature. This, however, requires further fundamental investigations in order to calibrate it or develop procedures to determine optimal values

20   dynamically. Moreover, the study shows that explicit sub-grid scale modelling is not necessarily required in lattice Boltzmann frameworks to capture the flow physics of wind turbine wakes, in line with previous studies using different Navier-Stokes discretisations (Sarlak et al., 2015a; Kleusberg et al., 2017; Deskos et al., 2019).

As for future applications of the lattice Boltzmann method to more realistic wind-power-related flow cases, the following conclusions can be drawn. First and foremost, the presented study underlines the suitability of the cumulant lattice Boltzmann

25   method for the simulation of highly turbulent engineering flows. The crucial advantage over other collision operators is the superior numerical stability of the method. No other collision operator initially tested in this study was found to be sufficiently robust using the given grid resolutions. The tested single- and multiple-relaxation-time models therefore do not appear suitable for LES of entire wind farms where higher spatial resolutions are not feasible and viscosities on the lattice scale consequently small. In summary, the advantages of the parametrised cumulant clearly render it as a preferable collision model for wind

30   turbine simulations and presumably other atmospheric flows. Application-oriented studies of the model are so far limited to this work and the recent study by Lenz et al. (2019). Further investigations of the model are therefore clearly required. This applies especially to the modelling of wall-bounded turbulent flows like atmospheric boundary layers. Furthermore, the presented work underlines the great potential of wind turbine simulations using the LBM. Without suffering losses in accuracy
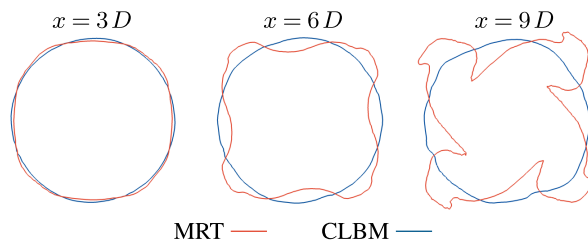
Figure A1. Instantaneous velocity contours ($u = 0.875\,u_0$) in cross-sectional planes at different positions in the wake of the turbine.

the computational cost can be significantly reduced when compared to standard NS-based approaches. In line with other discussions of the LBM (Löhner, 2019), the study shows that real-time LES of wind farms are feasible.

Code and data availability.   Both ELLIPSYS3D and ELBE are proprietary software and not publicly availabe. All data presented in this study can be made available upon request.

5 **Appendix A: Prestudy on the Stability of Collision Operators**

Generally, the choice of collision operator and lattice should consider stability, accuracy, memory demand and performance. Based on the seminal works by Geier et al. (2015, 2017b) the CLBM can undoubtedly be considered superior in terms of the former two. Utilising a D3Q27 lattice though eventually implies an increased memory demand of about 40%. Also, the higher complexity of the CLBM eventually renders the model computionally more expensive.

10   As for this specific set-up, satisfactory stability could only be achieved using the CLBM despite the use of the Smagorinsky model (for the referring formulations in moment space applied to the SRT and MRT models, see Yu et al. (2005, 2006)). The SRT generally became unstable after only a few time steps. The utilised MRT model (see, Tölke et al., 2006), on the other hand remained mostly numerically stable. Yet, unphysical oscillations in the turbulent regions of the flow led to significant degenerations throughout the entire domain.

15   In addition to stability issues, the isotropy of the D3Q19 lattice was shown to be insufficient. Fig. A1 shows three exemplary cross-stream velocity contours at different downstream positions. At $x = 3\,D$, small deviations from the expected axisymmetric profile can be observed for the MRT. Further downstream a more cross-like structure develops that deviates severely from an expanding circular wake. A similar behaviour on D3Q19 lattices has been described earlier by Geller et al. (2013) and Kang and Hassan (2013) when simulating circular jet and pipe flows, respectively. Both argue that the missing velocity vectors of the 20 D3Q19 lattice cause violations of the rotional invariance of axisymmetric flows. Furthermore, White and Chong (2011) remark that this behaviour might only be obvious when simulating simple axisymmetric flows, possibly with analytical reference solutions. Nevertheless, deteriorations of non-axisymmeric real-world problems should also be anticipated, yet, might be harder

to examine. This observation should thus also be taken into account when simulating wind turbines in more realistic, sheared, turbulent inflows.

Usually, stability issues as described above can be remedied by using smaller grid spacings. As we consider the latter unfeasible for the described applications, we refrain from further investigations thereof at this point. Moreover, White and
5 Chong (2011) also show that the lacking order of isotropy of the D3Q19 lattice can only partially be reduced under grid refinement. The use of the D3Q27 lattice and the CLBM thus appears as the most suitable choice for the investigation of wind turbine wakes. Lastly, it should be pointed out that performance differences between the investigated collision operators were only found to be around 15% (all simulations ran on a single Nvidia RTX 2080 Ti in single precision).

Appendix B: Local Computation of the Strain Rate Tensor in Cumulant Space

10 Following the asymptotic analysis of the CLBM given in Geier et al. (2015) the velocity derivatives are given as

$$\frac{\partial u}{\partial x} = -\frac{\omega_1}{2\rho}(2C_{200} - C_{020} - C_{002}) - \frac{\omega_2}{2\rho}(2C_{200} - C_{020} + \kappa_{000}) \tag{B1}$$

$$\frac{\partial v}{\partial y} = \frac{\partial u}{\partial x} + \frac{\omega_1}{2\rho}(2C_{200} - C_{020}) \tag{B2}$$

$$\frac{\partial w}{\partial z} = \frac{\partial u}{\partial x} + \frac{\omega_1}{2\rho}(2C_{200} - C_{002}) \tag{B3}$$

$$\frac{\partial v}{\partial x} + \frac{\partial u}{\partial y} = -\frac{3\omega_1}{2\rho}C_{110} \tag{B4}$$

15 $$\frac{\partial w}{\partial x} + \frac{\partial u}{\partial z} = -\frac{3\omega_1}{2\rho}C_{101} \tag{B5}$$

$$\frac{\partial w}{\partial y} + \frac{\partial v}{\partial z} = -\frac{3\omega_1}{2\rho}C_{011} \quad , \tag{B6}$$

where $C_{\alpha\beta\gamma} = \rho c_{\alpha\beta\gamma}$, with ρ being the fluid density. κ_{000} refers to the zeroth-order central velocity moment. The relaxation rate ω_1 relates to the total shear viscosity $\nu_{tot} = \nu + \nu_t$ as

$$\omega_1 = \left(\frac{3}{c^2}(\nu + \nu_t) + \Delta t/2\right)^{-1} \quad , \tag{B7}$$

20 following from Eq. (5). Due to ω_2, which is analogously linked to the bulk viscosity, Eq. (B7) can not be explicitly solved for ν_t. We therefore use $\nu_t(t - \Delta t)$ for the computation of the velocity derivatives at t as outlined in Sect. 2.3.

Since all cumulants as well as κ_{000} are readily available within the collision operator, the computation of $\bar{S}$ as given in the following comes at practically negligible computational cost:

$$\bar{S} = \left(2\left(\left(\frac{\partial u}{\partial x}\right)^2 + \left(\frac{\partial v}{\partial y}\right)^2 + \left(\frac{\partial w}{\partial z}\right)^2\right) + \left(\frac{\partial v}{\partial x} + \frac{\partial u}{\partial y}\right)^2 + \left(\frac{\partial w}{\partial x} + \frac{\partial u}{\partial z}\right)^2 + \left(\frac{\partial w}{\partial y}\right)^2 + \left(\frac{\partial v}{\partial y}\right)^2\right)^{\frac{1}{2}} \quad . \tag{B8}$$

25 Further details on the derivation of Eq. (B1) to Eq. (B6) can be found in Geier et al. (2017b).

Author contributions. HA developed and implemented the LBM-ALM, performed the simulations, post-processing and data analysis and drafted the original paper. HOE and SI contributed to the conceptualisation of the study, discussion of the results and revision of the manuscript.

Competing interests. The authors declare no coflict of interest.

References

Abkar, M.: Impact of Subgrid-Scale Modeling in Actuator-Line Based Large-Eddy Simulation of Vertical-Axis Wind Turbine Wakes, At-moshere, 9, 256, https://doi.org/doi:10.3390/atmos9070257, 2018.

Abkar, M. and Porté-Agel, F.: The Effect of Free-Atmosphere Stratification on Boundary-Layer Flow and Power Output from Very Large
5   Wind Farms, Energies, 6, 2338–2361, https://doi.org/10.3390/en6052338, 2013.

Abkar, M., Sharifi, A., and Porté-Agel, F.: Wake flow in a wind farm during a diurnal cycle, Journal of Turbulence, 17, 420–441, https://doi.org/10.1080/14685248.2015.1127379, 2016.

Ahmad, N. H., Inagaki, A., Kanda, M., Onodera, N., and Aoki, T.: Large-Eddy Simulation of the Gust Index in an Urban Area Using the Lattice Boltzmann Method, Boundary-Layer Meteorology, 163, 447–467, https://doi.org/10.1007/s10546-017-0233-6, 2017.

10   Andersen, S. J., Witha, B., Breton, S.-P., Sørensen, J. N., Mikkelsen, R. F., and Ivanell, S.: Quantifying variability of Large Eddy Simulations of very large wind farms, J. Phys. Conf. Ser., 625, 012 027, https://doi.org/10.1088/1742-6596/625/1/012027, 2015.

Andre, M., Mier-Torrecilla, M., and Wüchner, R.: Numerical simulation of wind loads on a parabolic trough solar collector us-ing lattice Boltzmann and finite element methods, Journal of Wind Engineering and Industrial Aerodynamics, 146, 185–194, https://doi.org/10.1016/j.jweia.2015.08.010, 2015.

15   Asmuth, H., Olivares-Espinosa, H., Nilsson, K., and Ivanell, S.: The Actuator Line Model in Lattice Boltzmann Frameworks: Numerical Sensitivity and Computational Performance, J. Phys. Conf. Ser., 1256, 012 022, https://doi.org/10.1088/1742-6596/1256/1/012022, 2019.

Avallone, F., van der Velden, W. C. P., Ragni, D., and Casalino, D.: Noise reduction mechanisms of sawtooth and combed-sawtooth trailing-edge serrations, Journal of Fluid Mechanics, 848, 560–591, https://doi.org/10.1017/jfm.2018.377, 2018.

Bauweraerts, P. and Meyers, J.: On the Feasibility of Using Large-Eddy Simulations for Real-Time Turbulent-Flow Forecasting in the
20   Atmospheric Boundary Layer, Boundary-Layer Meteorology, 171, 213–235, https://doi.org/10.1007/s10546-019-00428-5, 2019.

Bechmann, A., Sørensen, N. N., and Zahle, F.: CFD simulations of the MEXICO rotor, Wind Energy, 14, 677–689, https://doi.org/10.1002/we.450, http://dx.doi.org/10.1002/we.450, 2011.

Bhatnagar, P., Gross, E., and Krook, M.: A Model for Collision Processes in Gases. I. Small Amplitude Processes in Charged and Neutral One-Component Systems, Phys. Rev., 94, 511–525, https://doi.org/10.1103/PhysRev.94.511, 1954.

25   Bouzidi, M., Firdaouss, M., and Lallemand, P.: Momentum transfer of a Boltzmann-lattice fluid with boundaries, Physics of Flu-ids, 13, 3452–3459, https://doi.org/http://dx.doi.org/10.1063/1.1399290, http://scitation.aip.org/content/aip/journal/pof2/13/11/10.1063/1.1399290, 2001.

Buick, J. M. and Greated, C. A.: Gravity in a lattice Boltzmann model, Phys. Rev. E, 61, 5307–5320, https://doi.org/10.1103/PhysRevE.61.5307, 2000.

30   Churchfield, M., Lee, S., Moriarty, P., Martinez, L., Leonardi, S., Vijayakumar, G., and Brasseur, J.: A large-eddy simulation of wind-plant aerodynamics, in: Proceedings of the 50th AIAA Aerospace Sciences Meeting including the New Horizons Forum and Aerospace Exposition, p. 537, https://doi.org/10.2514/6.2012-537, 2012a.

Churchfield, M. J., Lee, S., Michalakes, J., and Moriarty, P. J.: A numerical study of the effects of atmospheric and wake turbulence on wind turbine dynamics, Journal of Turbulence, 13, N14, https://doi.org/10.1080/14685248.2012.668191, https://doi.org/10.1080/14685248.
35   2012.668191, 2012b.

Ciri, U., Rotea, M., Santoni, C., and Leonardi, S.: Large-eddy simulations with extremum-seeking control for individual wind turbine power optimization, Wind Energy, 20, 1617–1634, https://doi.org/10.1002/we.2112, 2017.

27

Deiterding, R. and Wood, S. L.: Predictive wind turbine simulation with an adaptive lattice Boltzmann method for moving boundaries, J. Phys.: Conf. Series, 753, 082 005, https://doi.org/10.1088/1742-6596/753/8/082005, 2016.

Dellar, P. J.: Bulk and shear viscosities in lattice Boltzmann equations, Phys. Rev. E, 64, 031 203, https://doi.org/10.1103/PhysRevE.64.031203, 2001.

5 Dellar, P. J.: Incompressible limits of lattice boltzmann equations using multiple relaxation times, J. Comput. Phys, p. 2003, https://doi.org/10.1016/S0021-9991(03)00279-1, 2003.

Deskos, G., Laizet, S., and Piggott, M. D.: Turbulence-resolving simulations of wind turbine wakes, Renewable Energy, 134, 989 –1002, https://doi.org/10.1016/j.renene.2018.11.084, 2019.

d'Humières, D., Ginzburg, I., Krafczyk, M., Lallemand, P., and Luo, L.-S.: Multiple-relaxation-time lattice Boltzmann models in three
10   dimensions, Philos. Trans. R. Soc. London, A, 360, 437–451, https://doi.org/10.1098/rsta.2001.0955, 2002.

Dilip, D. and Porté-Agel, F.: Wind Turbine Wake Mitigation through Blade Pitch Offset, Energies, 10, https://doi.org/10.3390/en10060757, 2017.

Fang, J., Peringer, A., Stupariu, M.-S., Pătru-Stupariu, I., Buttler, A., Golay, F., and Porté-Agel, F.: Shifts in wind energy potential following land-use driven vegetation dynamics in complex terrain, Sci. Tot. Environ., 639, 374–384, https://doi.org/10.1016/j.scitotenv.2018.05.083,
15   2018.

Far, E. K., Geier, M., Kutscher, K., and Krafczyk, M.: Simulation of micro aggregate breakage in turbulent flows by the cumulant lattice Boltzmann method, Comput. Fluids, 140, 222 – 231, https://doi.org/10.1016/j.compfluid.2016.10.001, 2016.

Fleming, P., Gebraad, P. M., Lee, S., Wingerden, J., Johnson, K., Churchfield, M., Michalakes, J., Spalart, P., and Moriarty, P.: Simulation comparison of wake mitigation control strategies for a two-turbine case, Wind Energy, 18, 2135–2143, https://doi.org/10.1002/we.1810,
20   2015.

Foti, D. and Duraisamy, K.: Implicit Large-Eddy Simulation of Wind Turbine Wakes and Turbine-Wake Interactions using the Vorticity Transport Equations, Proceedings of the AIAA Aviation 2019 Forum, https://doi.org/10.2514/6.2019-2841, 2019.

Fragner, M. and Deiterding, R.: Investigating cross-wind stability of high-speed trains with large-scale parallel CFD, International Journal of Computational Fluid Dynamics, 30, 402–407, https://doi.org/10.1080/10618562.2016.1205188, 2016.

25 Gehrke, M., Janßen, C., and Rung, T.: Scrutinizing lattice Boltzmann methods for direct numerical simulations of turbulent channel flows, Comput. Fluids, 156, 247–263, https://doi.org/10.1016/j.compfluid.2017.07.005, 2017.

Gehrke, M., Banari, A., and Rung, T.: Performance of Under-Resolved, Model-Free LBM Simulations in Turbulent Shear Flows, Notes on Numerical Fluid Mechanics and Multidisciplinary Design. Progress in Hybrid RANS-LES Modelling, 143, 3–18, https://doi.org/10.1007/978-3-030-27607-2_1, 2020.

30 Geier, M., Schönherr, M., Pasquali, A., and Krafczyk, M.: The cumulant lattice Boltzmann equation in three dimensions: Theory and valida-tion, Comput. Math. Appl., 70, 507–547, https://doi.org/10.1016/j.camwa.2015.05.001, 2015.

Geier, M., Pasquali, A., and Schönherr, M.: Parametrization of the cumulant lattice Boltzmann method for fourth order accurate diffusion part II: Application to flow around a sphere at drag crisis, J. Comput. Phys., 348, 889 – 898, https://doi.org/10.1016/j.jcp.2017.07.004, 2017a.

35 Geier, M., Pasquali, A., and Schönherr, M.: Parametrization of the cumulant lattice Boltzmann method for fourth order accurate diffusion part I: Derivation and validation, J. Comput. Phys., 348, 862–888, https://doi.org/10.1016/j.jcp.2017.05.040, 2017b.

Geller, S., Uphoff, S., and Krafczyk, M.: Turbulent jet computations based on MRT and Cascaded Lattice Boltzmann models, Computers & Mathematics with Applications, 65, 1956 –1966, https://doi.org/10.1016/j.camwa.2013.04.013, 2013.

Gilling, L.: TuGen: Synthetic Turbulence Generator, Manual and User's Guide, Tech. Rep. 76, Department of Civil Engineering, Aalborg University, 2009.

Gilling, L. and Sørensen, N. N.: Imposing resolved turbulence in CFD simulations, Wind Energy, 14, 661–676, https://doi.org/10.1002/we.449, 2011.

5 Ginzburg, I. and Adler, P.: Boundary flow condition analysis for the three-dimensional lattice Boltzmann model, J. Phys. II France, 4, 191–214, https://doi.org/10.1051/jp2:1994123, 1994.

Ginzburg, I., Verhaeghe, F., and d'Humières, D.: Two-Relaxation-Time Lattice Boltzmann Scheme: About Parametrization, Velocity, Pressure and Mixed Boundary Conditions, Commun. Comput. Phys., 3, 427–478, 2008.

Guo, Z., Zheng, C., and Shi, B.: Lattice Boltzmann equation with multiple effective relaxation times for gaseous microscale flow, Phys. Rev. E, 77, 036 707, https://doi.org/10.1103/PhysRevE.77.036707, 2008.

Hansen, M. O.: Aerodynamics of Wind Turbines, London, UK: Earthscan, 2008.

He, X. and Luo, L.-S.: Lattice Boltzmann Model for the Incompressible Navier–Stokes Equation, J. Stat. Phys., 88, 927–944, https://doi.org/10.1023/B:JOSS.0000015179.12689.e4, 1997.

Hong, P.-Y., Huang, L.-M., Lin, L.-S., and Lin, C.-A.: Scalable multi-relaxation-time lattice Boltzmann simulations on multi-GPU cluster, Computers & Fluids, 110, 1–8, https://doi.org/10.1016/j.compfluid.2014.12.010, 2016.

Hou, S., Sterling, J., Chen, S., and Doolen, D.: A Lattice Boltzmann Subgrid Model for High Reynolds Number Flows, in: Pattern Formation and Lattice Gas Automata, Fields Institute Com- munications, vol. 6, https://doi.org/arXiv:comp-gas/9401004, 1996.

Ivanell, S., Mikkelsen, R., Sørensen, J. N., and Henningson, D.: Stability Analysis of the Tip Vortices of a Wind Turbine, Wind Energy, 13, 705–715, https://doi.org/10.1002/we.391, 2010.

20 Ivanell, S., Arnqvist, J., Avila, M., Cavar, D., Chavez-Arroyo, R. A., Olivares-Espinosa, H., Peralta, C., Adib, J., and Witha, B.: Microscale model comparison (benchmark) at the moderate complex forested site Ryningsnäs, Wind Energ. Sci. Discussions, 2018, 1–27, https://doi.org/10.5194/wes-2018-20, 2018.

Jacob, J. and Sagaut, P.: Wind comfort assessment by means of large eddy simulation with lattice Boltzmann method in full scale city area, Build. Environ., 139, 110 – 124, https://doi.org/10.1016/j.buildenv.2018.05.015, 2018.

25 Jafari, S. and Mohammad, R.: Shear-improved Smagorinsky modeling of turbulent channel flow using generalized Lattice Boltzmann equation, International Journal for Numerical Methods in Fluids, 67, 700–712, https://doi.org/10.1002/fld.2384, 2011.

Janßen, C. F., Mierke, D., Überrück, M., Gralher, S., and Rung, T.: Validation of the GPU-Accelerated CFD Solver ELBE for Free Surface Flow Problems in Civil and Environmental Engineering, Computation, 3, 354, https://doi.org/10.3390/computation3030354, 2015.

Janßen, C. F., Mierke, D., and Rung, T.: On the development of an efficient numerical ice tank for the simulation of fluid-ship-rigid-ice inter-
30 actions on graphics processing units, Computers & Fluids, 155, 22 – 32, https://doi.org/10.1016/j.compfluid.2017.05.006, iCMMES2015, 2017.

Januszewski, M. and Kostur, M.: Sailfish: A flexible multi-GPU implementation of the lattice Boltzmann method, Computer Physics Communications, 185, 2350 – 2368, https://doi.org/10.1016/j.cpc.2014.04.018, 2014.

Jha, P. K., Churchfield, M. J., Moriarty, P. J., and Schmitz, S.: Guidelines for Volume Force Distributions Within Actuator Line Modeling of
35 Wind Turbines on Large-Eddy Simulation-Type Grids, J. Sol. Energy Eng., 136, 2013.

Jonkman, J., Butterfield, S., Musial, W., and Scott, G.: Definition of a 5-MW Reference Wind Turbine for Offshore System Development, Tech. Rep. NREL/TP-500-38060, NREL, 2009.

Kang, S. K. and Hassan, Y. A.: The effect of lattice models within the lattice Boltzmann method in the simulation of wall-bounded turbulent flows, Journal of Computational Physics, 232, 100 – 117, https://doi.org/10.1016/j.jcp.2012.07.023, 2013.

Keck, R.-E., Mikkelsen, R., Troldborg, N., de Maré, M., and Hansen, K. S.: Synthetic atmospheric turbulence and wind shear in large eddy simulations of wind turbine wakes, Wind Energy, 17, 1247–1267, https://doi.org/10.1002/we.1631, https://onlinelibrary.wiley.com/doi/abs/10.1002/we.1631, 2014.

Khan, A.: Finite element analysis of aerodynamic coefficients of a HAWT blade using LBM method, AIP Conference Proceedings, 1980, 040 007, https://doi.org/10.1063/1.5044317, 2018.

King, M.-F., Khan, A., Delbosc, N., Gough, H. L., Halios, C., Barlow, J. F., and Noakes, C. J.: Modelling urban airflow and natural ventilation using a GPU-based lattice-Boltzmann method, Build. Environ., 125, 273 – 284, https://doi.org/10.1016/j.buildenv.2017.08.048, 2017.

Kleusberg, E., Mikkelsen, R. F., Schlatter, P., Ivanell, S., and Henningson, D. S.: High-Order Numerical Simulations of Wind Turbine Wakes, J. Phys.: Conf. Series, 854, 012 025, https://doi.org/10.1088/1742-6596/854/1/012025, 2017.

Krafczyk, M., Tölke, J., and Luo, L.-S.: Large-eddy simulations with a multiple-relaxation-time LBE model, Int. J. Mod. Phys. B, 17, 33–39, https://doi.org/10.1142/S0217979203017059, 2003.

Krüger, T., Kusumaatmaja, H., Kuzmin, A., Shardt, O., Silva, G., and Viggen, E. M.: The Lattice Boltzmann Method - Principles and Practice, Heidelberg, Germany: Springer, 2016.

Kutscher, K., Geier, M., and Krafczyk, M.: Multiscale simulation of turbulent flow interacting with porous media based on a massively parallel implementation of the cumulant lattice Boltzmann method, Comput. Fluids, In Press, https://doi.org/10.1016/j.compfluid.2018.02.009, 2018.

Lallemand, P. and Luo, L.-S.: Theory of the lattice Boltzmann method: Dispersion, dissipation, isotropy, Galilean invariance, and stability, Phys. Rev. E, 61, 6546–6562, https://doi.org/10.1103/PhysRevE.61.6546, 2000.

Lallemand, P. and Luo, L.-S.: Lattice Boltzmann method for moving boundaries, Journal of Computational Physics, 184, 406–421, https://doi.org/http://dx.doi.org/10.1016/S0021-9991(02)00022-0, 2003.

Lenz, S., Schönherr, M., Geier, M., Krafczyk, M., Pasquali, A., Christen, A., and Giometto, M.: Towards real-time simulation of turbulent air flow over a resolved urban canopy using the cumulant lattice Boltzmann method on a GPGPU, Journal of Wind Engineering and Industrial Aerodynamics, 189, 151 – 162, https://doi.org/10.1016/j.jweia.2019.03.012, 2019.

Löhner, R.: Towards overcoming the LES crisis, International Journal of Computational Fluid Dynamics, 33, 87–97, https://doi.org/10.1080/10618562.2019.1612052, 2019.

Malaspinas, O. and Sagaut, P.: Advanced large-eddy simulation for lattice Boltzmann methods: The approximate deconvolution model, Physics of Fluids, 23, 105 103, https://doi.org/10.1063/1.3650422, 2011.

Malaspinas, O. and Sagaut, P.: Wall model for large-eddy simulation based on the lattice Boltzmann method, J. Comput. Phys., 275, 25 – 40, https://doi.org/10.1016/j.jcp.2014.06.020, 2014.

Mann, J.: Wind field simulation, Probabilist. Eng. Mech., 13, 269 – 282, https://doi.org/10.1016/S0266-8920(97)00036-2, 1998.

Martínez-Tossas, L. A., Churchfield, M. J., and Leonardi, S.: Large eddy simulations of the flow past wind turbines: actuator line and disk modeling, Wind Energy, 18, 1047–1060, https://doi.org/10.1002/we.1747, 2015.

Martínez-Tossas, L. A., Churchfield, M. J., Yilmaz, A. E., Sarlak, H., Johnson, P. L., Sørensen, J. N., Meyers, J., and Meneveau, C.: Comparison of four large-eddy simulation research codes and effects of model coefficient and inflow turbulence in actuator-line-based wind turbine modeling, J. Renewable Sustainable Energy, 10, 033 301, https://doi.org/10.1063/1.5004710, 2018.

Mehta, D., van Zuijlen, A., Koren, B., Holierhoek, J., and Bijl, H.: Large Eddy Simulation of wind farm aerodynamics: A review, J. Wind Eng. Ind. Aerodyn., 133, 1 – 17, https://doi.org/10.1016/j.jweia.2014.07.002, 2014.

Meng, H., Lien, F.-S., and Li, L.: Elastic actuator line modelling for wake-induced fatigue analysis of horizontal axis wind turbine blade, Renewable Energy, 116, 423 – 437, https://doi.org/10.1016/j.renene.2017.08.074, 2018.

5 Merlier, L., Jacob, J., and Sagaut, P.: Lattice-Boltzmann Large-Eddy Simulation of pollutant dispersion in street canyons including tree planting effects, Atmospheric Environment, 195, 89–103, https://doi.org/10.1016/j.atmosenv.2018.09.040, 2018.

Merlier, L., Jacob, J., and Sagaut, P.: Lattice-Boltzmann large-eddy simulation of pollutant dispersion in complex urban environment with dense gas effect: Model evaluation and flow analysis, Building and Environment, 148, 634–652, https://doi.org/10.1016/j.buildenv.2018.11.009, 2019.

10 Meyer Forsting, A. R., Pirrung, G. R., and Ramos-García, N.: A vortex-based tipsmearing correction for the actuator line, Wind Energ. Sci. Discuss., 2019, 1–22, 2019.

Michelsen, J. A.: Basis3D—A platform for development of multiblock PDE solvers, Tech. Rep. Report AFM 92-05, Technical University of Denmark, DTU, 1994a.

Michelsen, J. A.: Block structured multigrid solution of 2D and 3D elliptic PDE's, Tech. Rep. Report AFM 94-06, Technical University of Denmark, DTU, 1994b.

15 Mierke, D., Janßen, C., and Rung, T.: An efficient algorithm for the calculation of sub-grid distances for higher-order LBM boundary conditions in a GPU simulation environment, Comput. Math. Appl., https://doi.org/10.1016/j.camwa.2018.04.022, 2018.

Mohebbi, M. and Rezvani, M. A.: Multi objective optimization of aerodynamic design of high speed railway windbreaks using Lattice Boltzmann Method and wind tunnel test results, International Journal of Rail Transportation, 6, 183–201, https://doi.org/10.1080/23248378.2018.1463873, 2018.

20 Munters, W. and Meyers, J.: Dynamic Strategies for Yaw and Induction Control of Wind Farms Based on Large-Eddy Simulation and Optimization, Energies, 11, https://doi.org/10.3390/en11010177, 2018.

Nathan, J., Masson, C., and Dufresne, L.: Near-wake analysis of actuator line method immersed in turbulent flow using large-eddy simulations, Wind Energy Science, 3, 905–917, https://doi.org/10.5194/wes-3-905-2018, 2018.

25 Nathen, P., Haussmann, M., Krause, M., and Adams, N.: Adaptive filtering for the simulation of turbulent flows with lattice Boltzmann methods, Computers & Fluids, 172, 510 – 523, https://doi.org/10.1016/j.compfluid.2018.03.042, 2018.

Nebenführ, B. and Davidson, L.: Prediction of wind-turbine fatigue loads in forest regions based on turbulent LES inflow fields, Wind Energy, 20, 1003–1015, https://doi.org/10.1002/we.2076, 2017.

Nilsson, K., Ivanell, S., Hansen, K. S., Mikkelsen, R., Sørensen, J. N., Breton, S.-P., and Henningson, D.: Large eddy simulations of the Lillegrund wind farm, Wind Energy, 18, 449–467, https://doi.org/10.1002/we.1707, 2015.

30 Obrecht, C., Kuznik, F., Tourancheau, B., and Roux, J.-J.: Multi-GPU implementation of the lattice Boltzmann method, Comput. Math. Appl., 65, 252 – 261, https://doi.org/10.1016/j.camwa.2011.02.020, 2013.

Onodera, N. and Idomura, Y.: Acceleration of Wind Simulation Using Locally Mesh-Refined Lattice Boltzmann Method on GPU-Rich Supercomputers, in: Supercomputing Frontiers, edited by Yokota, R. and Wu, W., pp. 128–145, Springer International Publishing, 2018.

35 Onodera, N., Idomura, Y., Ali, Y., and Shimokawabe, T.: Communication Reduced Multi-time-step Algorithm for Real-time Wind Simulation on GPU-based Supercomputers, Proc. of the The International Conference for High Performance Computing, Networking, Storage, and Analysis, Dallas, USA, https://doi.org/10.1109/ScalA.2018.00005, 2018.

Pasquali, A., Geier, M., and Krafczyk, M.: Near-wall treatment for the simulation of turbulent flow by the cumulant lattice Boltzmann method, Comput. Math. Appl., p. In Press, https://doi.org/https://doi.org/10.1016/j.camwa.2017.11.022, https://www.sciencedirect.com/science/article/pii/S0898122117307484, 2017.

Porté-Agel, F., Wu, Y.-T., Lu, H., and Conzemius, R. J.: Large-eddy simulation of atmospheric boundary layer flow through wind turbines and wind farms, Journal of Wind Engineering and Industrial Aerodynamics, 99, 154 – 168, https://doi.org/https://doi.org/10.1016/j.jweia.2011.01.011, http://www.sciencedirect.com/science/article/pii/S0167610511000134, 2011.

Premnath, K. N., Pattison, M. J., and Banerjee, S.: Generalized lattice Boltzmann equation with forcing term for computation of wall-bounded turbulent flows, Phys. Rev. E, 79, 026 703, https://doi.org/10.1103/PhysRevE.79.026703, 2009a.

Premnath, K. N., Pattison, M. J., and Banerjee, S.: Dynamic subgrid scale modeling of turbulent flows using lattice-Boltzmann method, Physica A, 388, 2640–2658, https://doi.org/10.1016/j.physa.2009.02.041, 2009b.

Qian, Y.-H., D'Humières, D., and Lallemand, P.: Lattice BGK models for Navier-Stokes equation, Europhysics Letters, 17, 479, https://doi.org/10.1209/0295-5075/17/6/001, 1992.

Roache, P.: Verification of Codes and Calculations, AIAA Journal, 36, 696–702, 1998.

Rullaud, S., Blondel, F., and Cathelain, M.: Actuator-Line Model in a Lattice Boltzmann Framework for Wind Turbine Simulations, J. Phys.: Conf. Series, 1037, 022 023, https://doi.org/10.1088/1742-6596/1037/2/022023, 2018.

Sagaut, P.: Toward advanced subgrid models for Lattice-Boltzmann-based Large-eddy simulation: Theoretical formulations, Comput. Math. Appl., 59, 2194–2199, https://doi.org/10.1016/j.camwa.2009.08.051, 2010.

Sanderse, B., van der Pijl, S., and Koren, B.: Review of computational fluid dynamics for wind turbine wake aerodynamics, Wind Energy, 14, 799–819, https://doi.org/10.1002/we.458, 2011.

Sarlak, H.: Large Eddy Simulation of Turbulent Flows in Wind Energy, Ph.D. thesis, DTU Wind Energy, Denmark, 2014.

Sarlak, H., Meneveau, C., and Sørensen, J.: Role of subgrid-scale modeling in large eddy simulation of wind turbine wake interactions, Renewable Energy, 77, 386–399, https://doi.org/10.1016/j.renene.2014.12.036, 2015a.

Sarlak, H., Meneveau, C., Sørensen, J. N., and Mikkelsen, R.: Quantifying the Impact of Subgrid Scale Models in Actuator-Line Based LES of Wind Turbine Wakes in Laminar and Turbulent Inflow, in: Direct and Large-Eddy Simulation IX, edited by Fröhlich, J., Kuerten, H., Geurts, B. J., and Armenio, V., pp. 169–175, Springer International Publishing, Cham, 2015b.

Sarlak, H., Nishino, T., Martínez-Tossas, L., Meneveau, C., and Sørensen, J.: Assessment of blockage effects on the wake characteristics and power of wind turbines, Renewable Energy, 93, 340 – 352, https://doi.org/10.1016/j.renene.2016.01.101, 2016.

Sarmast, S., Dadfar, R., Mikkelsen, R. F., Schlatter, P., Ivanell, S., Sørensen, J. N., and Henningson, D. S.: Mutual inductance instability of the tip vortices behind a wind turbine, Journal of Fluid Mechanics, 755, 705–731, https://doi.org/10.1017/jfm.2014.326, 2014.

Schönherr, M., Kucher, K., Geier, M., Stiebler, M., Freudiger, S., and Krafczyk, M.: Multi-thread implementations of the lattice Boltzmann method on non-uniform grids for CPUs and GPUs, Comput. Math. Appl., 61, https://doi.org/10.1016/j.camwa.2011.04.012, 2011.

Sørensen, J. N. and Shen, W. Z.: Numerical Modeling of Wind Turbine Wakes, J. Fluids Eng., 124, 393–399, https://doi.org/10.1115/1.1471361, 2002.

Sørensen, J. N., Mikkelsen, R. F., Henningson, D. S., Ivanell, S., Sarmast, S., and Andersen, S. J.: Simulation of wind turbine wakes using the actuator line technique, Philosophical Transactions of the Royal Society of London A: Mathematical, Physical and Engineering Sciences, 373, 2015.

Sørensen, N. N.: General purpose flow solver applied to flow over hills, Ph.D. thesis, Risø National Laboratory, Roskilde, Denmark, 1995.

Storey, R., Cater, J., and Norris, S.: Large eddy simulation of turbine loading and performance in a wind farm, Renewable Energy, 95, 31 – 42, https://doi.org/10.1016/j.renene.2016.03.067, 2016.

Succi, S.: Lattice Boltzmann 2038, Europhysics Letters, 109, 50 001, https://doi.org/10.1209/0295-5075/109/50001, 2015.

Tölke, S., Freudiger, S., and Krafczyk, M.: An adaptive scheme using hierarchical grids for lattice Boltzmann multi-phase flow simulations,

5   Computers & Fluids, 35, 820–830, https://doi.org/10.1016/j.compfluid.2005.08.010, 2006.

Troldborg, N.: Actuator Line Modeling of Wind Turbine Wakes, Ph.D. thesis, Technical University of Denmark, Department of Mechanical Engineering, 2008.

Troldborg, N., Sørensen, J. N., and Mikkelsen, R.: Numerical simulations of wake characteristics of a wind turbine in uniform inflow, Wind Energy, 13, 86–99, https://doi.org/10.1002/we.345, 2010.

10   van der Velden, W., Pröbsting, S., van Zuijlen, A., de Jong, A., Guan, Y., and Morris, S.: Numerical and experimental investigation of a beveled trailing-edge flow field and noise emission, Journal of Sound and Vibration, 384, 113–129, https://doi.org/10.1016/j.jsv.2016.08.005, 2016.

Weickert, M., Teike, G., Schmidt, O., and Sommerfeld, M.: Investigation of the LES WALE turbulence model within the lattice Boltzmann framework, Comput. Math. Appl., 59, 2200–2214, https://doi.org/10.1016/j.camwa.2009.08.060, 2010.

15   White, A. T. and Chong, C. K.: Rotational invariance in the three-dimensional lattice Boltzmann method is dependent on the choice of lattice, Journal of Computational Physics, 230, 6367 – 6378, https://doi.org/10.1016/j.jcp.2011.04.031, 2011.

Yu, H., Girimaji, S. S., and Luo, L.-S.: DNS and LES of decaying isotropic turbulence with and without frame rotation using lattice Boltzmann method, Journal of Computational Physics, 209, 599 – 616, https://doi.org/10.1016/j.jcp.2005.03.022, 2005.

Yu, H., Luo, L.-S., and Girimaji, S. S.: LES of turbulent square jet flow using an MRT lattice Boltzmann model, Computers & Fluids, 35,

20   957–965, https://doi.org/10.1016/j.compfluid.2005.04.009, 2006.

Zhiqiang, L., Yunke, W., Jie, H., Zhihong, Z., and Wenqi, C.: The study on performance and aerodynamics of micro counter-rotating HAWT, Energy, 161, 939–954, https://doi.org/10.1016/j.energy.2018.07.049, 2018.